High external-efficiency nanofocusing for lens-free near-field optical nanoscopy

Sanggon Kim [1], Ning Yu[1], Xuezhi Ma [2], Yangzhi Zhu [1], Qiushi Liu [2], Ming Liu [2,3]★ and Ruoxue Yan [1,3]★

Efficient, broadband illumination and collection through a nanometre-sized hotspot carried by a scanning probe will endow light–matter interaction research with nanoscale spatial information. However, near-field scanning optical microscopy probes, particularly the high-resolution ones, demand cumbersome optics but can only concentrate less than 10^{-3} of the incident light, which has limited its applications. Here, we report a two-step sequential broadband nanofocusing technique with an external nanofocusing efficiency of ~50% over nearly all the visible range on a fibre-coupled nanowire scanning probe, which is capable of both light delivery and spectrum collection with nanoscale spatial resolution. By integrating this with a basic portable scanning tunnelling microscope, we have demonstrated lens-free tip-enhanced Raman spectroscopy and achieved 1 nm spatial resolution. The high performance and vast versatility offered by this fibre-based nanofocusing technique allow for the easy incorporation of nano-optical microscopy into various existing measurement platforms.

The extension of nanophotonics into the quantum regime requires the injection of photons into and extraction of photons from nanoscale dimensions with high spatial and spectral precision and low losses, which pushes the limits of our existing optical characterization tools not only in terms of spatial resolution but also in bandwidth and efficiency. The demand for deciphering light–matter interactions at the nanoscale has led to the invention and development of near-field scanning optical microscopy (NSOM), which defeats the diffraction limit by creating a nano-hotspot in the near-field[1–10]. However, despite many demonstrations of novel NSOM probe designs (such as tip-integrated bowtie antennas/apertures or concentric circle gratings at the tip[11–17]) to improve probe performance, the large mismatch in wavenumber k between the far-field propagating wave ($k \approx 10^5\,\mathrm{cm^{-1}}$ for visible wavelengths) and the highly confined localized-surface-plasmon mode (LSP, $k > 10^7\,\mathrm{cm^{-1}}$) at the near-field continues to pose a major challenge in the realization of broadband nanofocusing with high external efficiency[18]. Moreover, increasingly sophisticated probe fabrication, intricate instrument design and sensitive optical alignment have also limited the practical relevance of NSOM and its flexibility for integrating with other research platforms, such as ultrahigh-vacuum cryogenic systems and electron microscopes, to cater to the need for correlated spectroscopic, structural and even functional imaging at competing spatial resolutions.

An appealing method to smooth out the huge momentum gap between the far- and near-field is termed 'adiabatic nanofocusing'[8,19–27], the essence of which is to excite surface plasmon polaritons (SPPs) in a tapered waveguide that allows the SPPs to increase their wavenumbers gradually and smoothly as they propagate towards a nanosized tip to achieve efficient and broadband enhancement of the local field at the tip apex. This concept has been realized in tapered metal–insulator–metal (MIM) gap waveguides[5–7,28] and conical metal waveguides[24]. The former can compress linearly polarized incident light with high efficiency, but its

experimental resolution has been limited by fabrication restrictions. The latter, such as tapered metal tips and metal-coated fibres, utilize a radially polarized SPP mode (TM_0) excited through either a grating coupler[22–25] or the end-fire method[29,30], which can be adiabatically compressed to the tip apex[31,32]. However, its external nanofocusing efficiency—defined as the fraction of energy carried by the far-field incident photons that is effectively converted to the nanoscale LSP resonances—is currently limited to the lower single digit range. Practically, the most effective way to boost SPP excitation efficiency is the prism coupling method, which utilizes resonant mode coupling at the phase-matching condition for efficient energy transfer[33]. Unfortunately, although the incorporation of the phase-matching concept into nanofocusing NSOM probe design has long been considered promising[34–37], the experimental results are rather poor.

Results and discussion

In this Article, we demonstrate a two-step sequential nanofocusing technique to achieve high-efficiency, broadband and dual-directional nanofocusing for near-field optical excitation and spectrum collection. The nanofocusing process consists of two consecutive steps: (1) a resonant-mode-coupling process to selectively excite the TM_0 mode in a sharp-tip silver nanowire (AgNW) waveguide with the linearly polarized mode (LP_{01}) in a tapered optical fibre (OF) and (2) a quasi-adiabatic nanofocusing step to further compress the TM_0 mode through the chemically sharpened taper to the tip apex of the AgNW. Both steps have been accomplished with ~70% efficiencies, which combine to yield a total external nanofocusing efficiency of up to ~50% for both light injection and signal extraction across a broad range of the visible spectrum. The high-efficiency light shuttling between the far- and near-field, combined with the flexibility of the fibre-optics platform, has enabled the easy integration of such a AgNW-OF nanofocusing probe with commercial scanning probe microscopies. As a proof of concept, we converted a portable educational scanning tunnelling microscope (STM) (NatioSTM by

[1]Department of Chemical and Environmental Engineering, University of California, Riverside, Riverside, CA, USA. [2]Department of Electrical and Computer Engineering, University of California, Riverside, Riverside, CA, USA. [3]Materials Science and Engineering Program, University of California, Riverside, Riverside, CA, USA. *e-mail: mingliu@ucr.edu; rxyan@engr.ucr.edu
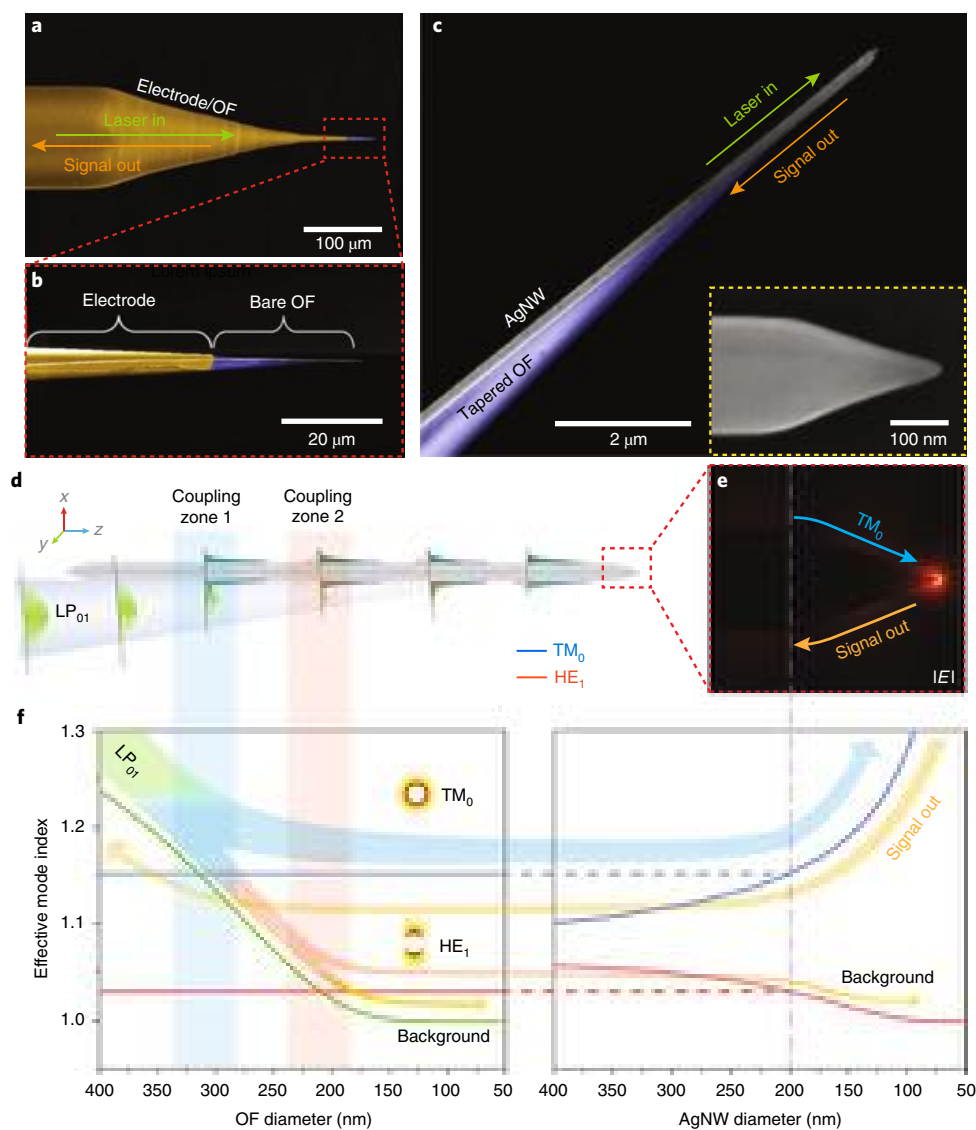
Fig. 1 | Two-step sequential nanofocusing concept. a–c, False-colour SEM images of a fabricated AgNW-OF probe, with a gold electrode (yellow) partially covering a tapered OF to electrically connect the AgNW for STM imaging. The OF tip region (blue) is uncovered for the selective and effective excitation of the TM_0 SPP on a sharp-tip silver nanowire (200 nm in diameter, ~5 nm in tip radius). Inset of **c**: enlarged view of the AgNW tip. **d**, The phase-matching zones for TM_0 and HE_1 modes are separated for the selective excitation of the former. **e**, Simulation of the nanofocusing at the AgNW tip (tip angle 37°), with TM_0 input from the left. The light wavelength is 532 nm for all calculations. **f**, Left: calculated effective mode index of the LP_{01} mode (green) with different OF diameters, and the mode indices of the TM_0 mode (blue line) and HE_1 mode (red line) of a AgNW (200 nm in diameter). Right: effective mode indices of the TM_0 mode (blue) and HE_1 mode (red) with different diameters. At the tapered AgNW tip, the TM_0 mode is further compressed by the reduced diameter.

Nanosurf) to a fibre-in–fibre-out (FIFO) lens-free STM-NSOM-TERS (tip-enhanced Raman spectroscopy) microscopy system capable of 1 nm imaging resolution and 208 c.p.s. (counts per second) sensitivity on single-walled carbon nanotubes (SWCNTs) and 1,520 c.p.s. on a Rhodamine 6G (R6G) monolayer.

Selective mode excitation and nanofocusing. The foundation of high-efficiency nanofocusing is the selective and efficient excitation of the radially polarized TM_0 mode, which is the only mode without cutoff and that can be effectively focused on the apex of a tapered rod, rather than higher-order loosely bound SPP modes on the AgNW (in particular the HE_1 SPP mode). In our design, the mode selectivity is accomplished by physically separating the coupling regions for different modes. Figure 1a–c presents scanning electron microscopy (SEM) images of a typical AgNW-OF probe.

A sharp-tip AgNW (5 nm tip radius, 200 nm diameter) sits on the sidewall of a tapered optical fibre (tip angle of ~6°), which is partially coated with a gold thin film (~100 nm thick; false-coloured in yellow) for the electrical connection required by the STM feedback control. The OF tip region starting ~30 μm from the fibre apex is left clean for SPP excitation. As shown in Fig. 1d–f, the incident light is launched into the fibre with linear polarization (p-LP_{01} mode, with the major E field along **x**) and evolves adiabatically along the tapered fibre tip, resulting in a gradual decrease in effective mode index (n_{OF}, green curve in Fig. 1f) and phase constant ($k_{OF} = n_{OF} \times k_0$, where k_0 is the vacuum wavenumber). When n_{OF} approaches the TM_0 mode index of the AgNW SPP (blue horizontal line, Fig. 1f) in coupling zone 1, the LP_{01}-TM_0 phase-matching condition is satisfied for resonant mode coupling between them. Consequently, most of the incident energy tunnels from the LP_{01} fibre mode to the TM_0
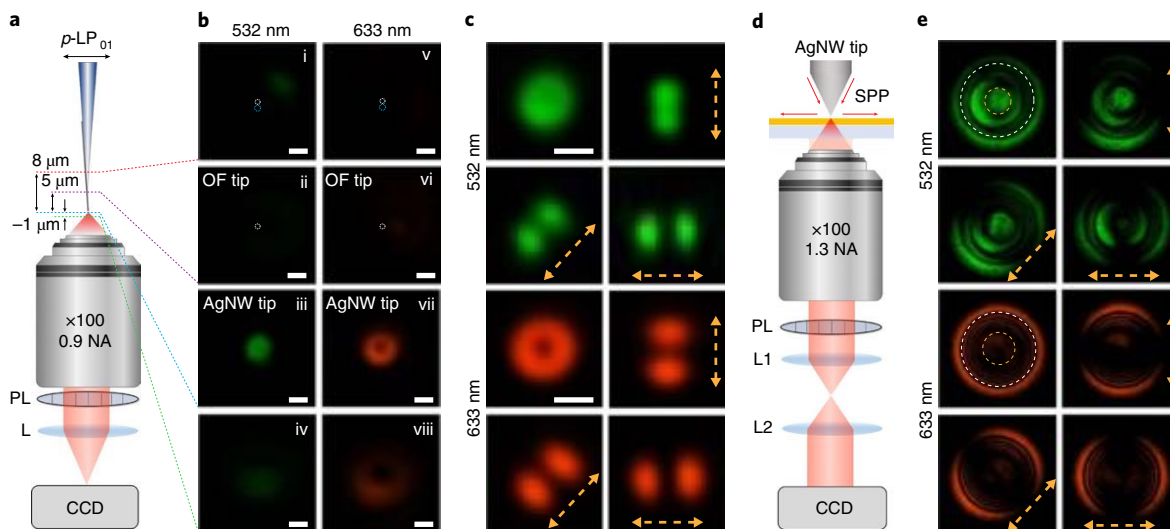
Fig. 2 | Experimental demonstration of selective and effective TM$_0$ mode excitation and nanofocusing. a,b, High-magnification optical microscope sectioning images taken under different excitation wavelengths (532 nm and 633 nm) by adjusting the focal plane of the imaging objective (×100, NA = 0.9) from different locations along the AgNW–OF probe: near the coupling zones (i,v); at the OF tip (ii,vi); at the AgNW tip (iii,vii); defocused by 1 μm (iv,viii). White and blue dashed circles indicate the locations of the AgNW and OF, respectively. **c,** Polarization-resolved images of **b** (iii) and (vii). Yellow dashed arrows illustrate the transmission axis of the polarization analyser (PL) placed in front of the lens (L) and CCD. Scale bars, 500 nm. **d,e,** Polarization-resolved *k*-space imaging of light emitted from the nanofocused SPP mode at the AgNW–OF probe apex, after transmitting through a thin gold film (~40 nm in thickness) deposited on a glass substrate. Strong rings outside the white dashed circle are the leaky SPP mode at the air–gold interface, excited by the nanofocused TM$_0$ mode. The linearly polarized pattern inside the orange dashed circle is from the free-space radiation of the HE$_1$ mode, attenuated by the gold film. The rings between the dashed circles are the attenuated radiation from the nanofocused TM$_0$ mode.

SPP mode. Beyond zone 1, the energy tunnelling terminates due to the mismatch in *k*, and the energy injected from the fibre is locked in the TM$_0$ SPP mode. This coupling process is an optical analogy to the Landau–Zener tunnelling effect[38], the efficiency of which is determined by the coupling strength and the variation rate of *k* along *z*, and can be as high as the Kretschmann–Raether configuration[33]. In a properly designed probe, only a small portion of the incident energy remains in the LP$_{01}$ fibre mode at this point, which propagates further to meet the resonant mode coupling conditions of the HE$_1$ mode in coupling zone 2. The existence of residue energy in either the HE$_1$ SPP mode or LP$_{01}$ fibre mode is highly undesirable, because neither can be effectively nanofocused at the AgNW tip due to mode cutoffs, and will both contribute to unwanted wide-field background illumination around the tip. Therefore, the efficiency of the energy tunnelling in zone 1 is essential in achieving effective nanofocusing with not only high efficiency but also low background noise. The second step of the nanofocusing process is illustrated in Fig. 1e. The TM$_0$ SPP mode, carrying the majority of the incident energy, is further compressed by the conical taper at the AgNW tip to a nanoscale LSP hotspot at the tip apex (Fig. 1e). This is a classic quasi-adiabatic nanofocusing process, which affords a compression efficiency of up to 70% for visible wavelengths (Supplementary Fig. 12) for the typical tip angle of the sharp-tip AgNW of ~40° (inset, Fig. 1c).

To experimentally verify the efficient and selective excitation of the TM$_0$ SPP mode in the AgNW, we performed vertical sectioning by shifting the focal plane of a high-numerical-aperture (NA = 0.9) objective lens along the probe axis from the AgNW–OF junction to the AgNW tip. Figure 2a presents the measurement set-up with the positions of the vertical sectioning marked; corresponding images under different excitation wavelengths are shown in Fig. 2b (for more images see Supplementary Information). For both 532 and 633 nm excitations, the scattered light from the AgNW–OF junction was close to zero (Fig. 2b(i),(ii) and (v),(vi)), confirming the high

coupling efficiency of the SPP launching process. This observation echoes a side-view image of the junction (Supplementary Fig. 5), which also shows negligible scattering loss during the process. The conclusive evidence of selective TM$_0$ excitation is shown in Fig. 2b(iii),(vii), where the AgNW tip apex appears as a single doughnut-shaped bright spot. As shown in the numerical simulations (Supplementary Fig. 8), this doughnut pattern is a signature of the TM$_0$ SPP mode and originates from the radially polarized far-field scattering of the tightly focused longitudinal dipole oscillating at the tip apex. The polarization-resolved images in Fig. 2c confirm that the radiated light from the AgNW tip is indeed radially polarized. In the case that the HE$_1$ mode dominates the OF-to-AgNW tunnelling process, which, for example, can be realized by changing the polarization of the fibre mode to the *s*-polarization (*s*-LP$_{01}$) that selectively excites the HE$_1$ SPP mode, a Gaussian-shaped spot was observed (Supplementary Fig. 8f).

The nanofocused TM$_0$ SPP mode at the AgNW tip apex was confirmed with spatially Fourier-transformed (*k*-space) imaging. As shown schematically in Fig. 2d, the AgNW tip was used to excite a leaky SPP mode at the air–gold interface of a gold-coated glass substrate, allowing resolution of the SPP modes at the tip apex through spatial Fourier transformation. The distance between the AgNW–OF probe and the gold film (40 nm in thickness) was kept at ~50 nm to maximize the excitation efficiency[39]. Figure 2e presents *k*-space images of the gold surface, acquired by projecting the objective's back-focal plane onto a charge-coupled device (CCD) camera. The radially polarized ring outside the white dashed circle is the leaky SPP mode excited by the nanofocused TM$_0$ mode. The partially radially polarized light between the orange and white dashed circles is also contributed by the nanofocused TM$_0$ mode, but by the portion that instead of exciting the leaky SPP modes along the gold surface is directly scattered into and propagated through the gold film. The weak linearly polarized beam inside the orange dashed circle is formed by the light scattered from the HE$_1$ mode at the AgNW tip apex and from the
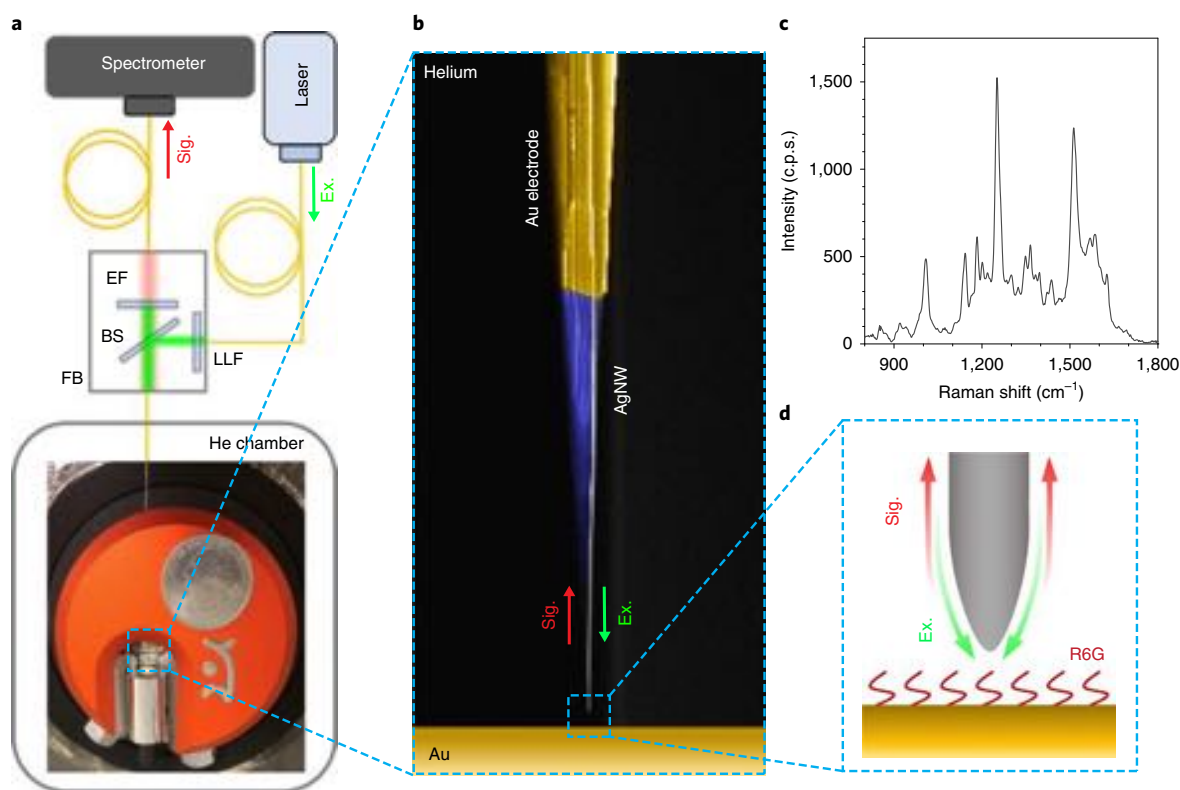
Fig. 3 | Lens-free STM-based FIFO-TERS. a, STM-based FIFO-TERS set-up, modified from a portable STM sealed in a helium chamber. The fibre-laser excitation light (Ex.) is collimated into free space at a fibre bench (FB), passes through a laser line filter (LLF), is reflected by a beamsplitter (BS) and is coupled into a short fibre (~20 cm), which conducts it through a helium chamber to reach the AgNW–OF probe for TERS excitation. The Raman signals are collected by the same probe, conveyed by the fibre back to the FB, filtered by an edge filter (EF) and carried by a signal fibre (Sig.) to the spectrometer for characterization. **b**, A false-colour SEM image shows an enlarged view of the AgNW–OF probe. **c**, A typical Raman spectrum of a R6G sample obtained with the FIFO (STM, 10 mV, 2 nA; Raman, 1 μW, 5 s). **d**, Schematic of the FIFO-TERS configuration near the probe tip. All Raman spectra in this work were corrected by subtracting the CCD noise.

LP_{01} mode residue at the OF tip apex, passing through the gold-coated glass slide and collected by the CCD. The k-space imaging shows unambiguously that the TM_0 mode is dominant at both the 532 nm and 633 nm excitations, demonstrating efficient TM_0 mode nanofocusing by the AgNW tip.

FIFO-NSOM STM-TERS. The high-efficiency, mode-selective, broad-bandwidth and dual-directional nanofocusing, combined with the flexible and lens-free nature of the fibre-optic platform, enables the easy incorporation of near-field nanoscopy into existing high-resolution research platforms. TERS, for example, is a powerful tool to deliver chemical information at molecular length scales[40,41]. However, after nearly two decades of development, it is still considered an esoteric technique by many due to its complex instrumentation, difficult optical alignment and probe fabrication (necessary to achieve high resolution and sensitivity). With the fibre-based nanofocusing probe, we have shown that a basic educational STM can be converted to a high-performance portable TERS without resorting to cumbersome optical systems and delicate alignment procedures (Fig. 3a). This is the first demonstration of lens-free TERS and a major step towards making it a practical tool for routine nanochemical imaging. The STM module was sealed in a set of glass chambers filled with helium gas, which protected the AgNW from being oxidized and also reduced the environmental sound noise level via acoustic impedance mismatch. Both the excitation laser (532 nm solid-state laser) and Raman signals (~550–590 nm) were conveyed in and out of the chamber via the same

piece of single-mode optical fibre (Model SM600, Thorlabs, ~20 cm length). The fibre had a tapered tip fabricated using a programmable fibre etching system through a two-step meniscus etching process (for details see Supplementary Section 6), which creates a thick, stable base to maximize the mechanical stability of the probe and a sharp tip with optimized taper angle θ_{OF} for high-efficiency TM_0 coupling (Fig. 1a). As mentioned earlier, the optical fibre was partially coated with a 100-nm-thick gold film to electrically connect the AgNW for tunnelling-current feedback control, which maintains a roughly 1 nm tip-to-substrate distance during scanning. Consequently, a plasmonic gap cavity is maintained between the tip apex and the metal substrate, which creates a nanometre-sized hotspot for high-resolution TERS excitation. The gap hotspot can also strongly increase the radiative decay rate for the emitters in its vicinity. Moreover, finite element method simulation revealed that the short-range energy transfer to the gap SPP mode dominated the radiation process for a Raman emitter in the gap (for details see Supplementary Section 5). Therefore, instead of being scattered into free space, the majority of the Raman signals are coupled back into the TM_0 SPP mode in the AgNW and collected by the optical fibre through the high-efficiency broadband back-coupling process. The Raman spectra were separated from the incident laser by a fibre-bench beamsplitter, filtered by a long-pass edge filter, and then fed to a high-sensitivity thermoelectric-cooled CCD detector. The integration of a FIFO nanofocusing TERS module with the STM requires minimal modification to the commercial scanning probe microscopy system or optical alignments (Supplementary Fig. 16).
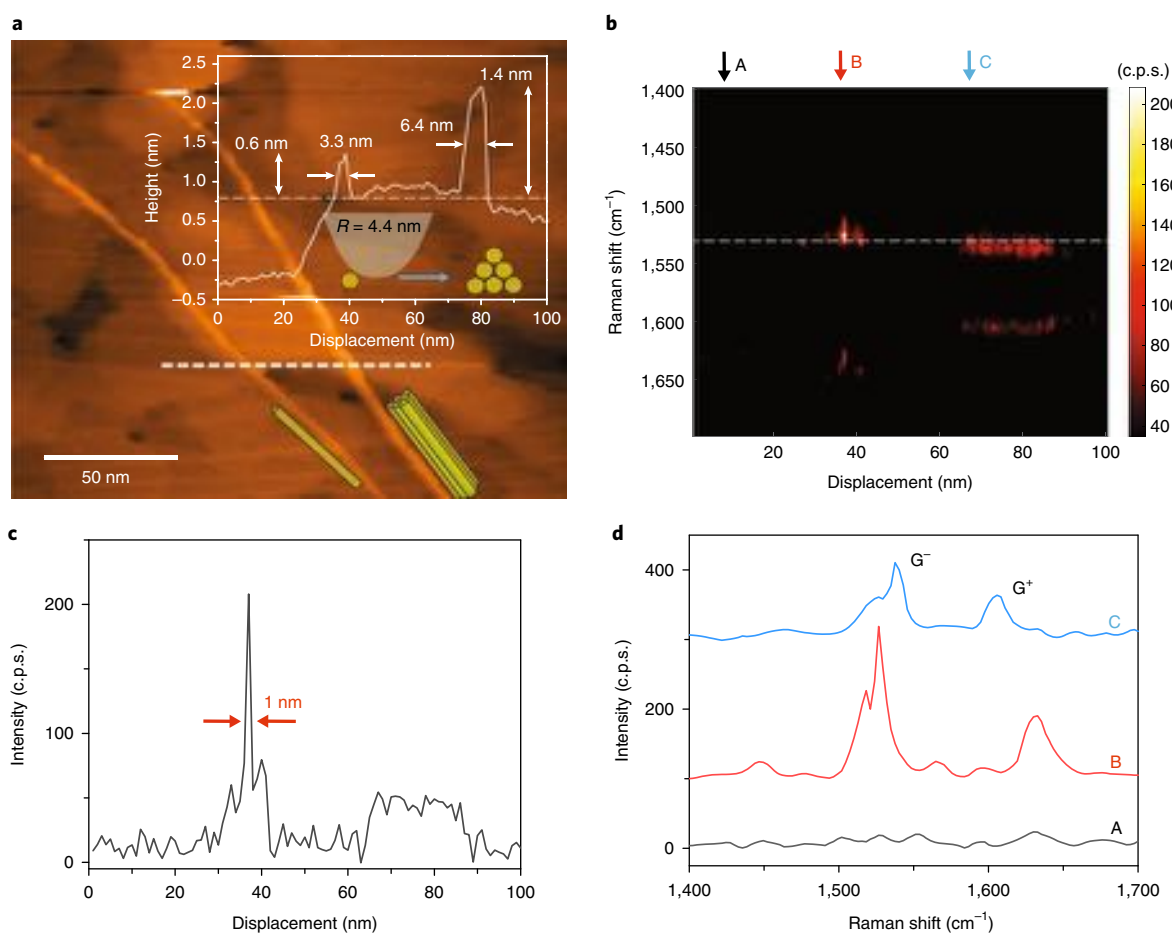
Fig. 4 | High-resolution FIFO-TERS mapping. a, STM topographic image of SWCNTs on a Au film. Top inset: cross-sectional profile along the dashed line. Bottom inset: the possible configurations of the bundle. **b**, 2D plot of Raman spectra obtained along the white dashed line in **a**. **c**,**d**, Intensity of the Raman peak at 1,526 cm^{-1} along the white dashed line in **a**. Arrows in **c** indicate the position of the Raman spectra in **d**. The used tunnelling current and bias voltage are 0.5 nA and 1 V, respectively. The Raman acquisition time of each spectrum is 1 s (532 nm, ~1 μW).

Owing to the low-loss nanofocusing and signal collection, high-quality Raman spectra can be collected on a self-assembled mono-layer of molecular Raman dye sample (Fig. 3c), a reference sample commonly used for TERS sensitivity evaluation[42]. With an incident power of merely 1 μW, a Raman signal intensity ~1,520 c.p.s. was achieved. The exclusion of high-power laser and intricate optical focusing systems not only significantly simplifies the equipment and operation for high-quality TERS measurements, but also makes it practical to incorporate high-resolution chemical mapping capability into vacuum-chamber-based platforms.

The spatial resolution of the FIFO nanofocusing probe for both STM and TERS mapping was examined with SWCNTs deposited on Au. Figure 4a presents an STM topographic mapping of the sample, which clearly shows two SWCNT bundles. The height profile extracted along the white dashed line (top right inset) shows the left bundle has a height of 0.6 nm and a full-width at half-maximum (FWHM) of 3.3 nm, while the right one has a height of 1.4 nm and an FWHM of 6.4 nm. Taking into account of the 0.8 nm average diameter of the SWCNT sample, the left bundle at the dashed line is composed of a single SWCNT that is 0.6 nm in diameter; from this and the FWHM we estimate the tip radius of the probe to be ~4.4 nm, which is in good agreement with SEM measurements (Fig. 1c). The right bundle consists of multiple SWCNTs and the cartoon in Fig. 4a shows a possible configuration of six SWCNTs with hexagonal close-packed stacking, based on the height and FWHM.

Along the same dashed line, a TERS line scan was performed and the Raman spectra at different positions were plotted in a 2D image (Fig. 4b). The spectra exhibit two clear bands at ~1,540 cm^{-1} and ~1,600–1,630 cm^{-1} at positions that correspond well with the STM line scan (Fig. 4d). The former peak is assigned to the G$^-$ band, consistent with the confocal Raman spectrum. The latter is assigned to the G$^+$ band, which is considerably redshifted (more so in the single SWCNT on the left than the bundle on the right) compared to the confocal Raman spectrum (~1,580–1,590 cm^{-1}), which may be a result of the torsional strain exerted by the probe tip[43,44], the dynamic temperature variation[45] and the nanoscale cavity effect[46] (Supplementary Section 6). Figure 4c plots the intensity (in c.p.s.) of the G$^-$ peak as a function of the position, and an FWHM of 1 nm was achieved on the single SWCNT, which indicates the spatial resolution of the FIFO nanofocusing probe for TERS chemical mapping. In addition, for the same single SWCNT, a peak height of 208 c.p.s. was also demonstrated. It is also worth noting that 70% of the SWCNTs in the commercial SWCNT used in our test were semiconducting, which compelled us to choose a bias higher than their ~0.6 V bandgap and that potentially limited the TERS signal attainable.

Coupled-mode evolution. To further understand the selective TM$_0$ mode excitation and dual-directional broad-bandwidth coupling, improved coupled-mode theory[47] was implemented to investigate
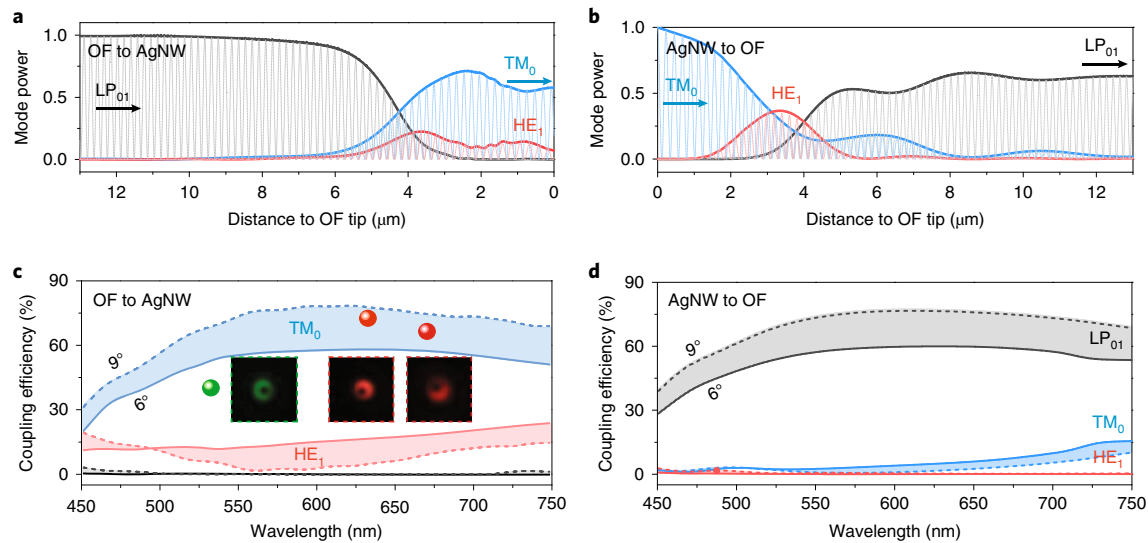
Fig. 5 | Mode evolution in the separate-region resonant mode coupling process. a,b, Mode power evolution along the AgNW-OF coupler for the forward (OF to AgNW) and backward (AgNW to OF) coupling processes, respectively ($\theta_{OF} = 7°$, $\lambda = 532$ nm, $d_{AgNW} = 200$ nm). **c**, Dependence of the forward coupling efficiencies of TM_0 (blue) and HE_1 (red) modes on wavelength, with θ_{OF} varying from 6° (solid curves) to 9° (dashed curves). Inset: tip scattering images for 532, 633 and 671 nm excitation. **d**, Dependence on wavelength of the backward coupling efficiency from the TM_0 mode to the OF.

the evolution of different modes in the AgNW and the OF along their junction using the following general expression:

$$dA_m/dz = ik_m A_m + \sum_{m,n} iK_{mn} A_n \qquad (1)$$

where m, n represent the three participating modes (LP_{01}, TM_0 and HE_1), A_m are the normalized electromagnetic fields and k_m are the phase constants. K_{mn} ($m=n$) represents the modification to k_i from the neighbouring waveguide, and K_{mn} ($m \neq n$) represents the modified coupling coefficients from mode n to mode m (see Supplementary Information). Polarization of the LP_{01} mode was set along the x direction (p-polarization) to achieve a non-zero coupling coefficient with the TM_0 mode. The orthogonal polarization (s-LP_{01}) plays no role here because the selection rule forbids the coupling of the s-LP_{01} mode with the TM_0 of the AgNW and it will only excite the undesirable HE_1 mode. Figure 5a shows the mode intensity evolution along the coupled waveguides during the nanofocusing process, with excitation in the LP_{01} fibre mode (532 nm) sent from the left. Energy tunnelling from the OF to the AgNW starts at ~6 μm from the fibre tip, marked by a rapid drop in the LP_{01} mode intensity. Because the LP_{01}-TM_0 phase-matching condition is satisfied first, the TM_0 mode picks up the majority of the input power. As a result, little energy is left in the LP_{01} mode when the phase-matching condition for HE_1 coupling is finally established. Within 4 μm of coupling, above 99% of the incident energy is channelled into the AgNW, with ~70% remaining in the TM_0 mode at the OF tip ($z=0$) when plasmonic loss is included.

The effective signal extraction from a nanoconfined region, a reverse process of nanofocusing, also relies on the resonant mode coupling. Figure 5b shows the mode evolution in the back-coupling process, as the onset of the energy tunnelling from the TM_0 mode in the AgNW. In this reverse process, the TM_0 mode is first coupled to the HE_1 mode through a process similar to the stimulated Raman adiabatic passage (STIRAP) in coupled waveguides[48], where two waveguide modes (TM_0 and HE_1) utilize a third mode in a different waveguide (for example, the leaky LP_{01} fibre mode) as a bridge to exchange mode power. The optical power temporarily stored in the HE_1 mode is later coupled back into the LP_{01} mode in their

phase-matching zone. The mode-power changing rate derived from mode-coupling theory is in good agreement with the Poynting flux extracted from the numerical simulation.

The AgNW–OF coupler has a broad working bandwidth covering the majority of the visible spectrum owing to the forgiving phase-matching conditions established by the gradual taper of the coupling region. Figure 5c,d presents the calculated forward and backward coupling efficiencies in the visible wavelength range for the OF taper angle (θ_{OF}) of 6–9°. The optimization of θ_{OF} is essential in achieving high-efficiency, dual-directional, mode-selective and broadband LP_{01}–TM_0 coupling, because it determines the distance and degree of overlapping between two coupling zones. A large θ_{OF} reduces the inter-zone distance and leads to the early onset of the LP_{01}–HE_1 coupling process, which interrupts the TM_0 mode excitation process and reduces its weight in total optical power. A small θ_{OF}, on the other hand, results in a long propagation distance for the TM_0 mode before it reaches the OF tip and thus a high propagation loss. Our calculation indicates that within the optimized θ_{OF} of ~7–12° (see Supplementary Information), both the forward and backward coupling of the TM_0 mode can be achieved with ~60–70% external coupling efficiency in the entire green and red wavelength range.

We performed Fourier-transform k-space imaging measurements of the AgNW tip to experimentally quantify the weight of the TM_0 mode and determine the external coupling efficiency; these confirm that the AgNWs with diameter of ~200 nm have the highest TM_0 mode selectivity (Supplementary Fig. 3). The efficiency for the TM_0 mode can be calculated from the experimental mode weight, leading to 40%, 72% and 66% for 532, 633 and 671 nm excitations, respectively, which are plotted in Fig. 5c and are in good agreement with the mode-coupling theory.

Conclusions

In summary, we have demonstrated a two-step sequential optical nanofocusing method for fibre-based near-field optical nanoscopy. We have experimentally shown that one in every two incident photons can be effectively focused onto a nano-hotspot at the apex of a nanowire probe. This technique combines the advantages of both scattering- and aperture-NSOM, by providing strong signal

enhancement and a clean optical background without resorting to cumbersome optical focusing systems. In addition, its broadband and dual-directional nature also allows for near-field spectrum collection at a nanometre length scale. The high performance and flexibility of the system can convert a basic educational STM to the first lens-free TERS with 1 nm resolution and up to 1,520 c.p.s. signal strength at ≤1 µW of incident power, which represents a major step towards bringing TERS, a powerful but esoteric molecular imaging tool, to its full potential. By offering an easy solution for efficiency light injection and/or extraction at a nanometre length scale, fibre-based near-field nanoscopy holds great potential as a plug-in module for existing high-resolution measurement platforms to provide complementary and spatially correlated information on molecular compositions (for example, TERS), material properties (for example, inter- and intraband transitions) and optoelectronic device performance (for example, photocurrent mapping).

Online content

Any methods, additional references, Nature Research reporting summaries, source data, statements of code and data availability and associated accession codes are available at https://doi.org/10.1038/s41566-019-0456-9.

Data availability

The data that support the plots within this paper and other findings of this study are available from the corresponding authors upon reasonable request.

References

1. Betzig, E., Trautman, J., Harris, T., Weiner, J. & Kostelak, R. Breaking the diffraction barrier: optical microscopy on a nanometric scale. *Science* **251**, 1468–1470 (1991).
2. Novotny, L. in *Progress in Optics* Vol. 50 (ed. Wolf, E.) Ch. 5, 137–184 (Elsevier, 2007).
3. Kawata, S., Inouye, Y. & Verma, P. Plasmonics for near-field nano-imaging and superlensing. *Nat. Photon.* **3**, 388–394 (2009).
4. Rotenberg, N. & Kuipers, L. Mapping nanoscale light fields. *Nat. Photon.* **8**, 919–926 (2014).
5. Choi, H., Pile, D. F. P., Nam, S., Bartal, G. & Zhang, X. Compressing surface plasmons for nano-scale optical focusing. *Opt. Express* **17**, 7519–7524 (2009).
6. Bao, W. et al. Mapping local charge recombination heterogeneity by multidimensional nanospectroscopic imaging. *Science* **338**, 1317–1321 (2012).
7. Choo, H. et al. Nanofocusing in a metal–insulator–metal gap plasmon waveguide with a three-dimensional linear taper. *Nat. Photon.* **6**, 837–843 (2012).
8. Kravtsov, V., Ulbricht, R., Atkin, J. & Raschke, M. B. Plasmonic nanofocused four-wave mixing for femtosecond near-field imaging. *Nat. Nanotechnol.* **11**, 459–464 (2016).
9. Hillenbrand, R., Taubner, T. & Keilmann, F. Phonon-enhanced light–matter interaction at the nanometre scale. *Nature* **418**, 159–162 (2002).
10. Keilmann, F. Surface-polariton propagation for scanning near-field optical microscopy application. *J. Microsc.* **194**, 567–570 (1999).
11. Wang, L. & Xu, X. High transmission nanoscale bowtie-shaped aperture probe for near-field optical imaging. *Appl. Phys. Lett.* **90**, 261105 (2007).
12. Burresi, M. et al. Probing the magnetic field of light at optical frequencies. *Science* **326**, 550–553 (2009).
13. Wang, Y., Srituravanich, W., Sun, C. & Zhang, X. Plasmonic nearfield scanning probe with high transmission. *Nano Lett.* **8**, 3041–3045 (2008).
14. Srituravanich, W. et al. Flying plasmonic lens in the near field for high-speed nanolithography. *Nat. Nanotechnol.* **3**, 733–737 (2008).
15. Zhao, Y. et al. Nanoscopic control and quantification of enantioselective optical forces. *Nat. Nanotechnol.* **12**, 1055–1059 (2017).
16. Schuller, J. A. et al. Plasmonics for extreme light concentration and manipulation. *Nat. Mater.* **9**, 193–204 (2010).
17. Novotny, L. & Van Hulst, N. Antennas for light. *Nat. Photon.* **5**, 83–90 (2011).
18. Gramotnev, D. K. & Bozhevolnyi, S. I. Plasmonics beyond the diffraction limit. *Nat. Photon.* **4**, 83–91 (2010).
19. Pile, D. & Gramotnev, D. K. Adiabatic and nonadiabatic nanofocusing of plasmons by tapered gap plasmon waveguides. *Appl. Phys. Lett.* **89**, 041111 (2006).
20. Vernon, K. C., Gramotnev, D. K. & Pile, D. F. Adiabatic nanofocusing of plasmons by a sharp metal wedge on a dielectric substrate. *J. Appl. Phys.* **101**, 104312 (2007).
21. Stockman, M. I. Nanofocusing of optical energy in tapered plasmonic waveguides. *Phys. Rev. Lett.* **93**, 137404 (2004).
22. Giugni, A. et al. Hot-electron nanoscopy using adiabatic compression of surface plasmons. *Nat. Nanotechnol.* **8**, 845–852 (2013).
23. Berweger, S., Atkin, J. M., Olmon, R. L. & Raschke, M. B. Adiabatic tip-plasmon focusing for nano-Raman spectroscopy. *J. Phys. Chem. Lett.* **1**, 3427–3432 (2010).
24. Ropers, C. et al. Grating-coupling of surface plasmons onto metallic tips: a nanoconfined light source. *Nano Lett.* **7**, 2784–2788 (2007).
25. Jiang, R. H. et al. Near-field plasmonic probe with super resolution and high throughput and signal-to-noise ratio. *Nano Lett.* **18**, 881–885 (2018).
26. Nerkararyan, K. V. Superfocusing of a surface polariton in a wedge-like structure. *Phys. Lett. A* **237**, 103–105 (1997).
27. Tuniz, A. & Schmidt, M. A. Broadband efficient directional coupling to short-range plasmons: towards hybrid fiber nanotips. *Opt. Express* **24**, 7507–7524 (2016).
28. Schnell, M. et al. Nanofocusing of mid-infrared energy with tapered transmission lines. *Nat. Photon.* **5**, 283–287 (2011).
29. Chen, X. W., Sandoghdar, V. & Agio, M. Highly efficient interfacing of guided plasmons and photons in nanowires. *Nano Lett.* **9**, 3756–3761 (2009).
30. Tuniz, A., Chemnitz, M., Dellith, J., Weidlich, S. & Schmidt, M. A. Hybrid-mode-assisted long-distance excitation of short-range surface plasmons in a nanotip-enhanced step-index fiber. *Nano Lett.* **17**, 631–637 (2017).
31. Gramotnev, D. K., Vogel, M. W. & Stockman, M. I. Optimized nonadiabatic nanofocusing of plasmons by tapered metal rods. *J. Appl. Phys.* **104**, 034311 (2008).
32. Issa, N. A. & Guckenberger, R. Optical nanofocusing on tapered metallic waveguides. *Plasmonics* **2**, 31–37 (2007).
33. Raether, H. *Surface Plasmons on Smooth and Rough Surfaces and on Gratings* (Springer, 1988).
34. Tugchin, B. N. et al. Plasmonic tip based on excitation of radially polarized conical surface plasmon polariton for detecting longitudinal and transversal fields. *ACS Photon.* **2**, 1468–1475 (2015).
35. Bouhelier, A., Renger, J., Beversluis, M. & Novotny, L. Plasmon-coupled tip-enhanced near-field optical microscopy. *J. Microsc.* **210**, 220–224 (2003).
36. Janunts, N., Baghdasaryan, K., Nerkararyan, K. V. & Hecht, B. Excitation and superfocusing of surface plasmon polaritons on a silver-coated optical fiber tip. *Opt. Commun.* **253**, 118–124 (2005).
37. Barthes, J., des Francs, G. C., Bouhelier, A. & Dereux, A. A coupled lossy local-mode theory description of a plasmonic tip. *New J. Phys.* **14**, 083041 (2012).
38. Novotny, L. Strong coupling, energy splitting and level crossings: a classical perspective. *Am. J. Phys.* **78**, 1199–1202 (2010).
39. Becker, S. F. et al. Gap-plasmon-enhanced nanofocusing near-field microscopy. *ACS Photon.* **3**, 223–232 (2016).
40. Schmid, T., Opilik, L., Blum, C. & Zenobi, R. Nanoscale chemical imaging using tip-enhanced Raman spectroscopy: a critical review. *Angew. Chem. Int. Ed.* **52**, 5940–5954 (2013).
41. Sonntag, M. D., Pozzi, E. A., Jiang, N., Hersam, M. C. & Van Duyne, R. P. Recent advances in tip-enhanced Raman spectroscopy. *J. Phys. Chem. Lett.* **5**, 3125–3130 (2014).
42. Yeo, B. S., Stadler, J., Schmid, T., Zenobi, R. & Zhang, W. Tip-enhanced Raman spectroscopy—its status, challenges and future directions. *Chem. Phys. Lett.* **472**, 1–13 (2009).
43. Yano, Ta et al. Tip-enhanced nano-Raman analytical imaging of locally induced strain distribution in carbon nanotubes. *Nat. Commun.* **4**, 2592 (2013).
44. Liao, M. et al. Tip-enhanced Raman spectroscopic imaging of individual carbon nanotubes with subnanometer resolution. *Nano Lett.* **16**, 4040–4046 (2016).
45. Piscanec, S., Lazzeri, M., Robertson, J., Ferrari, A. C. & Mauri, F. Optical phonons in carbon nanotubes: Kohn anomalies, Peierls distortions and dynamic effects. *Phys. Rev. B* **75**, 035427 (2007).
46. Benz, F. et al. Single-molecule optomechanics in 'picocavities'. *Science* **354**, 726–729 (2016).
47. Chuang, S. L. *Physics of Optoelectronic Devices* (Wiley, 1995).
48. Vitanov, N., Fleischhauer, M., Shore, B. & Bergmann, K. Coherent manipulation of atoms and molecules by sequential laser pulses. *Adv. Atom. Mol. Opt. Phys.* **46**, 55–190 (2001).

Author contributions

Competing interests

The authors declare no competing interests.

Additional information

Supplementary information is available for this paper at https://doi.org/10.1038/s41566-019-0456-9.

Reprints and permissions information is available at www.nature.com/reprints.

Correspondence and requests for materials should be addressed to M.L. or R.Y.

Publisher's note: Springer Nature remains neutral with regard to jurisdictional claims in published maps and institutional affiliations.

In the format provided by the authors and unedited.

High external-efficiency nanofocusing
for lens-free near-field optical nanoscopy

Sanggon Kim [1], **Ning Yu**[1], **Xuezhi Ma** [2], **Yangzhi Zhu** [1], **Qiushi Liu** [2], **Ming Liu** [2,3]*
and Ruoxue Yan [1,3]*

[1]Department of Chemical and Environmental Engineering, University of California, Riverside, Riverside, CA, USA. [2]Department of Electrical and Computer Engineering, University of California, Riverside, Riverside, CA, USA. [3]Materials Science and Engineering Program, University of California, Riverside, Riverside, CA, USA. *e-mail: mingliu@ucr.edu; rxyan@engr.ucr.edu

Supplementary Information:

High external-efficiency nanofocusing for lens-free near-field optical nanoscopy

Sanggon Kim[1], Ning Yu[1], Xuezhi Ma[2], Yangzhi Zhu[1], Qiushi Liu[2], Ming Liu[2,3*] and Ruoxue Yan[1,3*]

Addresses:

[1]Department of Chemical and Environmental Engineering, University of California, Riverside, California 92521, United States

[2]Department of Electrical and Computer Engineering, University of California, Riverside, California 92521, United States

[3]Materials Science and Engineering program, University of California, Riverside, California 92521, United States

Corresponding author information: mingliu@ucr.edu, rxyan@engr.ucr.edu

Table of Contents

1. Rigorous analysis of the AgNW-OF mode coupling process

1.1 Improved coupled-mode theory

In the AgNW-OF hybrid waveguide system, the surface plasmon polariton (SPP) modes in the AgNW waveguide are strongly coupled with the fiber mode in the tapered OF since two waveguides are closely packed. Therefore, the widely used coupled-mode theory that considers only the weak coupling between two separated waveguides is insufficient in accuracy. Following the rigorous derivation in the Appendix H in Ref [1], we developed codes based on the improved coupled-mode theory that considers not only the mode-coupling coefficient between two waveguides, but also the butt coupling coefficient and the change in propagation constant. Now the general evolution of the three modes (two SPP modes—TM_0, HE_1, and one OF mode—LP_{01} is determined by the following generalized coupled-mode equations[1]:

$$\frac{d}{dz}\begin{pmatrix} a(z) \\ b(z) \\ c(z) \end{pmatrix} = i \begin{pmatrix} k_a + K_{aa} & K_{ab} & K_{ac} \\ K_{ba} & k_b + K_{bb} & 0 \\ K_{ca} & 0 & k_c + K_{cc} \end{pmatrix} \begin{pmatrix} a(z) \\ b(z) \\ c(z) \end{pmatrix} \qquad S(1)$$

Here, $a(z)$, $b(z)$ and $c(z)$ are the normalized amplitudes of the electromagnetic field of mode LP_{01}, TM_0 and HE_1, respectively. k_i ($i = a, b, c$) is the modified propagation constant, K_{ij} is the modified coupling coefficient from mode j to mode i, and K_{ii} is the modification to k_i due to the existence of the neighbor waveguide. Their detailed expressions can be found in Appendix H in Ref [1]. It is worth noting that since the TM_0 mode is orthogonal to the HE_1 mode, the coupling coefficient $K_{bc} = K_{cb} = 0$ throughout the simulation.

Because the diameter of the tapered OF changes at different z, k_i, K_{ii}, and K_{ij} are also functions of z. Their values are calculated from the overlapping integrals of the corresponding electromagnetic field distributions, which are obtained from the mode analysis performed by the finite element method (COMSOL Multiphysics). To prepare k_i, K_{ii}, and K_{ij} for eq. $S(1)$, the fundamental LP_{01} mode in an OF with a diameter ranging from 10 nm to 900 nm is calculated, at a dynamic step size between 5nm to 30nm. For the diameter smaller than the cut-off diameter, the mode with the highest mode refractive index is adapted.

The differential equations in eq.$S(1)$ are calculated using an ordinary differential equation (ODE) solver (Matlab Mathworks, ode45). To simulate the forward coupling process (from fiber to AgNW), the initial condition $(1, 0, 0)^T$ was used to represent the population in the OF in eq. $S(1)$. The origin point of z (z = 0) in the ODE solver is set at $r_{SiO2} = 900\ nm$, and the end

boundary is set at $r_{SiO2} = 0\,nm$. To simulate the backward coupling process (from the AgNW TM$_0$ mode to the OF), the initial condition is $(0,\ 1,\ 0)^T$, and the origin point of z is set at $r_{SiO2} = 0\,nm$, with the ending point set at $r_{SiO2} = 900\,nm$.

1.2 Role of the separation of coupling regions in the selective excitation and its angle dependence

The selective excitation of the TM$_0$ mode rather than the HE$_1$ mode is realized by separating their coupling regions. Because the TM$_0$ mode always have a higher effective mode index ($n_{eff} = k_b/k_0$, k_0 is the propagation constant in vacuum) than other SPP modes, the incident light in the tapered OF runs into the phase-matching region for the TM$_0$ mode first, where $k_a = k_b$ (let the corresponding fiber radius be r_{TM0}). The uncoupled light remaining in the OF propagates to the phase-matching region for HE$_1$ mode, where its phase constant matches with k_c. Modes higher than HE$_1$ are not supported by the narrow diameter used in this experiment at the visible wavelength[2], and are not considered here. The distance d between the two coupling regions is related to the tapered angle θ_{OF}, through the equation:

$$d \approx 2(r_{TM0} - r_{HE1})/\theta_{OF} \qquad\qquad S(2)$$

here r_{TM0} and r_{HE1} are the corresponding radii of the OF at the phase matching regions. Therefore, by changing the fiber tip angle θ_{OF}, the separation distance between two coupling regions can be varied. Figure S1a shows the exit mode powers of TM$_0$ and HE$_1$, and the uncoupled light (which turns into a free-space propagating wave and becomes the background noise), at different fiber tip angle (θ_{OF}). As shown by the evolution of mode power in Figure S1c, a large θ_{OF} (15°) reduces the weight of TM$_0$ mode because of the early introduction of the LP$_{01}$-to-HE$_1$ tunneling process. On the other hand, a small θ_{OF} also reduces the overall transmittance of TM$_0$ mode due to the large plasmonic loss (~0.3dB/μm) [3] after the long propagation distance from the coupling region to the tapered fiber apex. The optimized fiber tip angle for the coupling of 532nm excitation into a 200nm-in-diameter AgNW is between 7°~12°.

To further demonstrate the role of the separation distance between coupling regions (d) in the selective mode excitation, we reduce d to zero by setting k_c equal to k_b and check its influence on the mode evolution process. The same parameters used in Figure S1b are recalculated and depicted in Figure S1d. It clearly shows that in the new evolution, both the TM$_0$ mode (red) and the HE$_1$ mode (yellow) start to grow at the same position (~6μm from the fiber tip), where the phase matching condition $k_a = k_b = k_c$ is satisfied. Since the HE$_1$ mode has a linearly-polarized mode profile and consequently a larger overlapping integral with the

linearly-polarized LP_{01} mode, its mode power increases faster than the TM_0 mode power. This simulation unequivocally reveals that the separation of the coupling regions is the key in realizing the selective excitation of the TM_0 mode.
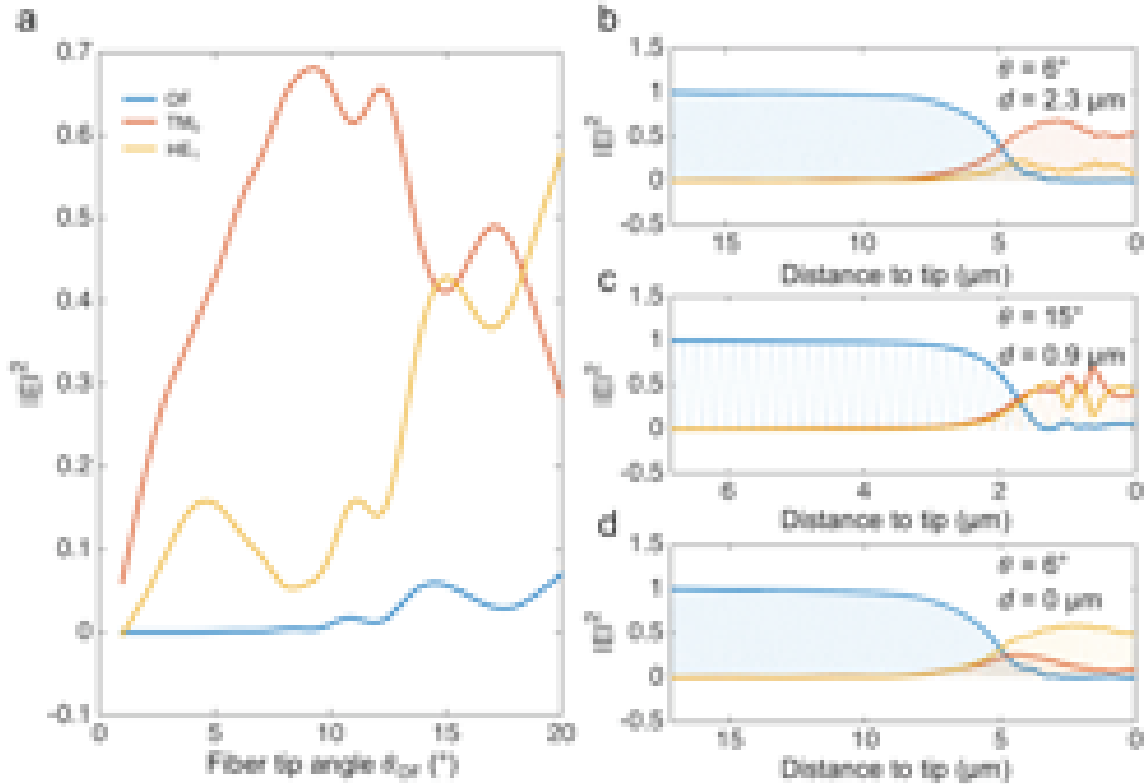
Figure S1 | The role of seperation of couping regions in the selective excitation of the TM_0 mode. *(a)*, Mode powers at the fiber tip. The optimized angle for TM_0-mode excitation is 7° ~ 12°. *(b)* and *(c)*, The evolution of mode power in the waveguides for 6° and 15° fiber tip angle, respectively. The 15° tip cannot excite TM_0 mode efficiently, since the two coupling regions are not sperated far enough. *(d)*, To evaluate the role of seperation of coupling regions, the phase matching regions for TM_0 and HE_1 are set the same, by forcing k_c equal to k_b (then $d = 0$), while remaining other parameters the same as used in *(b)*. The HE_1 mode dominates after the coupling process. In all simulations, the diameter of AgNW is 200 nm, and the excitation wavelength is 532 nm.

1.3 Improved coupled-mode theory validity check

We employ three methods to validate the accuracy of the improved coupled-mode theory:

full-wave numerical simulation, mode decomposition, and far-field k-space measurement.

1.3.1 Comparison with full-wave numerical simulation

Figure S2 shows the comparison between the 3D numerical simulation results achieved by the finite element analysis (COMSOL Multiphysics) and the calculated mode evolution from the coupled mode theory. Limited by the computing capability, the length of the AgNW was set to ~ 4~5 μm and the whole simulation domain was ~ 7μm in length in the simulations. The left end of the short AgNW induces most of the scattering in Figure S2a, which could be avoided if longer AgNWs were used. The fiber tip angle θ_{OF} was set at 9° to move the coupling regions to around 4 μm away from the fiber tip ($z = 0$). As shown in Figure S2a and d, simulations confirm that both the forward (OF to AgNW) and backward (AgNW to OF) coupling processes can deliver a large portion of the incident power to the adjacent waveguide. The vertical component of the time-averaged Poynting vector ($<S_x>$, Figure S2b and e) depicts the optical energy flux
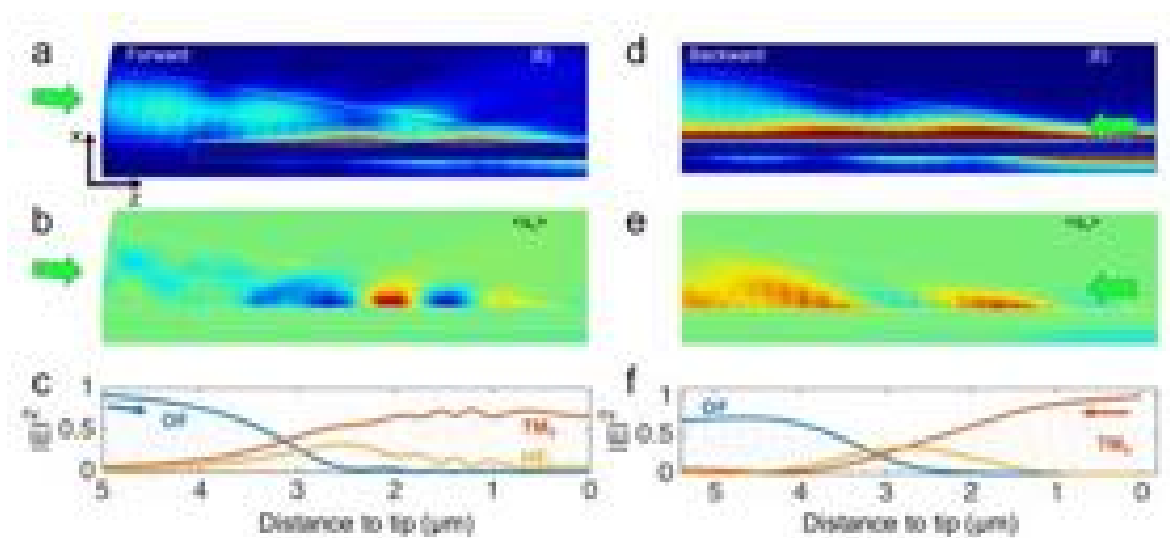
Figure S2 | Comparison between numerical simulations and the coupled-mode theory. *(a)* and *(d)***,** The E-field distribution for the forward (OF to AgNW) and backward (AgNW to OF) coupling process, acquired by 3D FEA simulations. In *(d)***,** TM_0 mode is launched on the right-end of the AgNW. *(b)* and *(e)***,** The vertical component of the Poynting vector illustrates the coupling regions. *(c)* and *(f)***,** The mode evolution given by the improved coupled-mode theory. In all simulations, the diameter of AgNW is 200 nm, and the excitation wavelength is 532 nm.

along $\vec{x}$, which represents the optical power exchange between the three participating modes. For example, the blue region at around $z = 3$ μm in Figure S2b indicates that strong optical tunneling occurs from the OF downward to the AgNW, which agrees with the mode evolution in Figure S2c, where the fiber mode power (blue curve) starts to decline at around 3 μm. Similar correspondence is found in the backward coupling process. The fiber mode power starts to rise at around 3.5 μm in the back-coupling process (blue curve in Figure S2f), which corresponds to a red region in Figure S2e. It is worth noting that the power exchange between the TM_0 mode and HE_1 mode can also be observed in $<S_x>$, since they have different intensity profiles and their coupling induces energy redistribution within the plane perpendicular to the AgNW waveguide. The TM_0-HE_1 coupling arises near the fiber tip (between 1 to 3 μm), which generates a red and a blue region in Figure S2b and a red region centered at 1.5 μm in Figure S2e. This coupling process is similar to the stimulated Raman adiabatic passage (STIRAP) in waveguides[4,5], where two waveguide modes (here TM_0 and HE_1) utilizes a third waveguide (here the leaky OF mode) as a bridge to exchange powers. The optical energy temporarily stored in the HE_1 mode is later coupled into the OF as well, at its phase-matching region.

In all the numerical calculations in this work, the optical property of Ag was adopted from Johnson's & Christy's Data[6], and the permittivity and Young's modulus of SiO_2 are 2.15 and 70 GPa, respectively.

1.3.2 Comparison with mode decomposition method

In order to verify the accuracy of the improved coupled-mode theory, we perform numerical investigations in COMSOL Multiphysics for the mode weight analysis. All fields at the cross-section of AgNW protruding region can be decomposed in term of azimuthal mode number m, by using the Fourier series:

$$E_{\rho,z,\phi}(\rho, z, \phi) = \sum_m E_{\rho,z,\phi}^{(m)}(\rho, z)e^{im\phi} \qquad\qquad S(3)$$

Since the AgNW has a rotational symmetry that is ϕ-independent, each cylindrical harmonic mode propagates independently after leaving the AgNW-fiber junction region. The full vector equations $S(3)$ can be solved on the 2D cross-section near the tip of the AgNW for the amplitude of each m (Figure S3b). We find that within the interested wavelength range, only the first three SPP modes on AgNW (TM_0, HE_1, and HE_{-1}) need to be considered, which verifies the choosing of these modes in the improved coupled-mode theory. Figure S3c shows the fitted results, where the composition of the first three modes (dashed line) fits well with the $|E_z|$
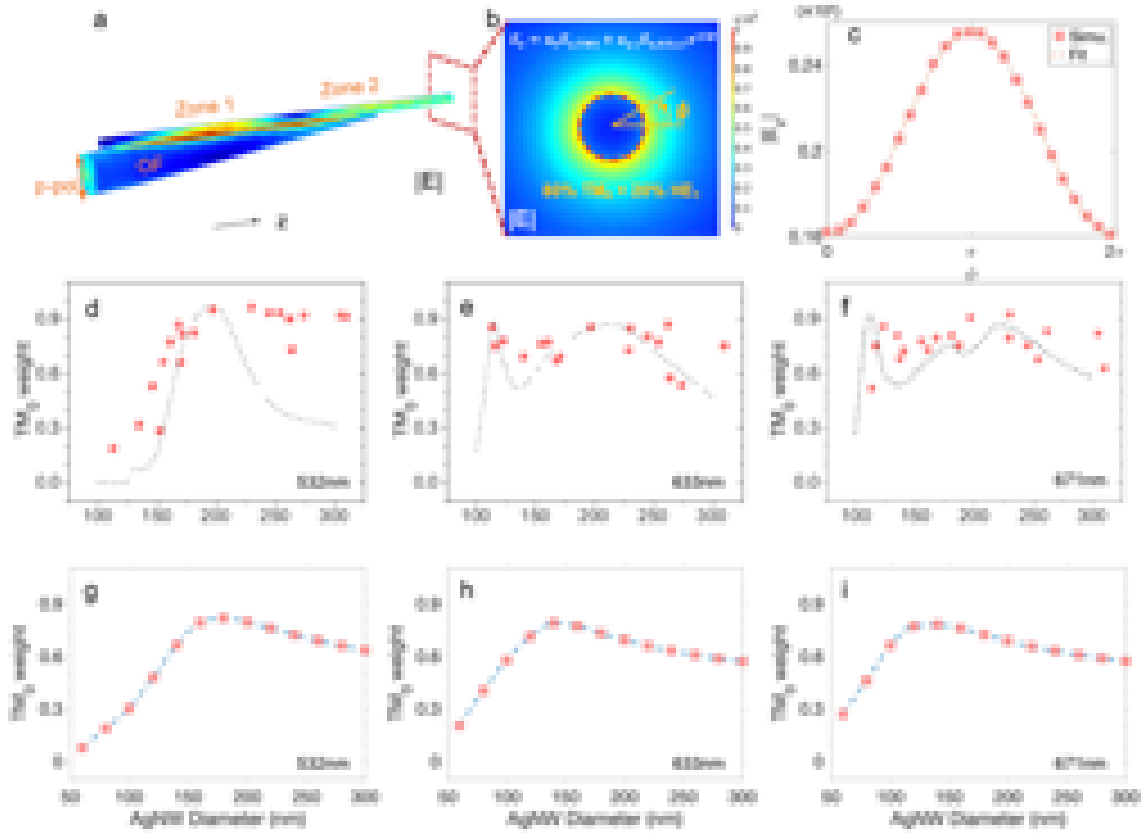
Figure S3| Numerical and experimental demonstration of the TM$_0$ mode excitation. a, Electric field distribution at the AgNW-OF probe surface. p-LP01 mode excitation is launched from the optical fiber, towards the tapered tip (taper angle 8°). The overlapping distance between the AgNW (180nm in diameter) and the optical fiber is 5 μm. **b**, Cross-section of the simulated |E| field near the end of the AgNW. The near-radially-symmetric field distribution contains 80% (in power-weight) of TM$_0$ mode and 20% of HE$_{\pm1}$ mode. **c**, The simulated E$_z$ magnitude (red squares) along the AgNW surface (red dashed line in **b**) can be decomposed into three modes: TM$_0$, HE$_{+1}$, and HE$_{-1}$. The total power of these three modes (dashed curve) fits well with the simulation data (red squares). **d~f**, TM$_0$ mode power weights acquired by k-space measurement (red dots) and the improved coupled mode theory (dotted curve). **g~i**, TM$_0$ mode weights acquired by the mode-decomposition method.

8

Figure S4. Spatial Fourier transformed far-field radiation pattern (k-space) measurement.

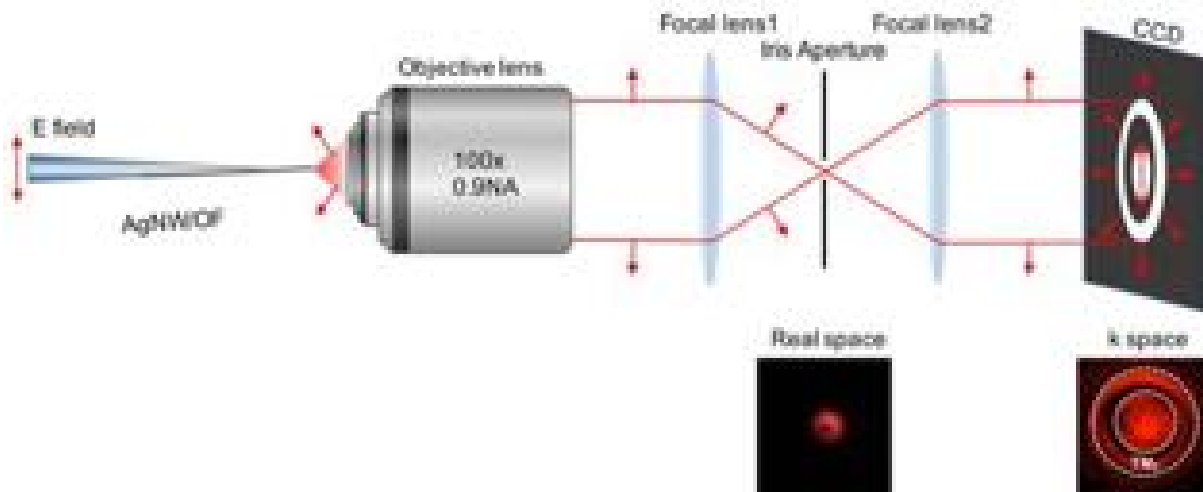component along the surface of the AgNW at the cross-section. The mode powers can be calculated by integrating Poynting flux, which can be calculated using all field vectors derived from E_z. Figure S3 g~i depict the calculated TM_0 mode power weights for different wavelengths, which agree well with the improved coupled-mode theory (short-dashed curves) and experimental results (red squares) in Figure S3 d~f, particularly in the large-diameter (> 200nm) region. This mode-decomposition method is less accurate for small diameter AgNWs, mainly because that small-diameter AgNWs have high mode effective indices for TM0 mode, which requires the fiber with large diameters for the phase-matching condition. This requires the AgNW-OF overlapping distance longer than 5 μm, which cannot be performed due to the extremely heavy computational load. Despite this limitation, the mode-decomposition method still in general agrees with the experimental data and theoretical results, demonstrates the validity of the improved coupled-mode theory, and proves the efficient excitation of TM_0 mode under proper designs.

1.3.3 Comparison with experimental data

The k-space measurement is carried out on an upright optical microscope that has been modified by introducing an iris aperture at the imaging plane, as sketched in Figure S4. The AgNW probe is placed in front of the objective lens, with its axis perpendicular to the focal plane. Light scattered from the AgNW tip apex is collected with a high numerical aperture objective (NA=0.9). The spatial Fourier transform of light is imaged by a s-CMOS CCD (Zyla 5.5, Andor)

camera placed at the front focal plane of the focal lens 2.

The far-field radiation of the TM_0 mode forms a radially polarized beam, as explained in the previous section. Consequently, when focused to the image plane by a low NA lens ($f = 10cm$), the transverse E-field component dominates at the focused spot and forms a ring pattern[7] (Figure S4 bottom-left inset). In the k-space, the TM_0 mode forms the radially polarized ring, while the HE_1 mode forms a spot in the center.

The k-space image can be used to analyze the weight/power of each mode and also the external coupling efficiency in the AgNW waveguide, after considering their collection efficiencies. The mode weights for different AgNW diameter at various wavelengths are shown in Figure S3 d~f.

1.4 Scattering loss during the coupling process

1.4.1 Side-scattering loss

In the improved coupled-mode modeling, the scattering loss from the OF to the free space is ignored, and only three modes (LP_{01}, TM_0, and HE_1) are considered. This assumption is valid if the scattering loss is low and negligible.

Beside of the cross-section images shown in Figure 2, we also examined the side-view of the AgNW-OF coupler, as shown in Figure S5. The dark-field optical image in Figure S5a depicts the location of the AgNW on the tapered fiber. The AgNW tip of the free-standing end acts as a strong scattering spot when the 532nm laser is sent in through the OF. The intensity profiles recorded by a s-CMOS charged-coupled device (CCD, Zyla 5.5, Andor) camera are shown in Figure S5c and under logarithmic scale in Figure S3d (to highlight the scattered light), which confirm that the tip intensity is more than 2 orders higher than the scattered light. This experimental result agrees with the numerical simulation result shown in Figure S5e and f.
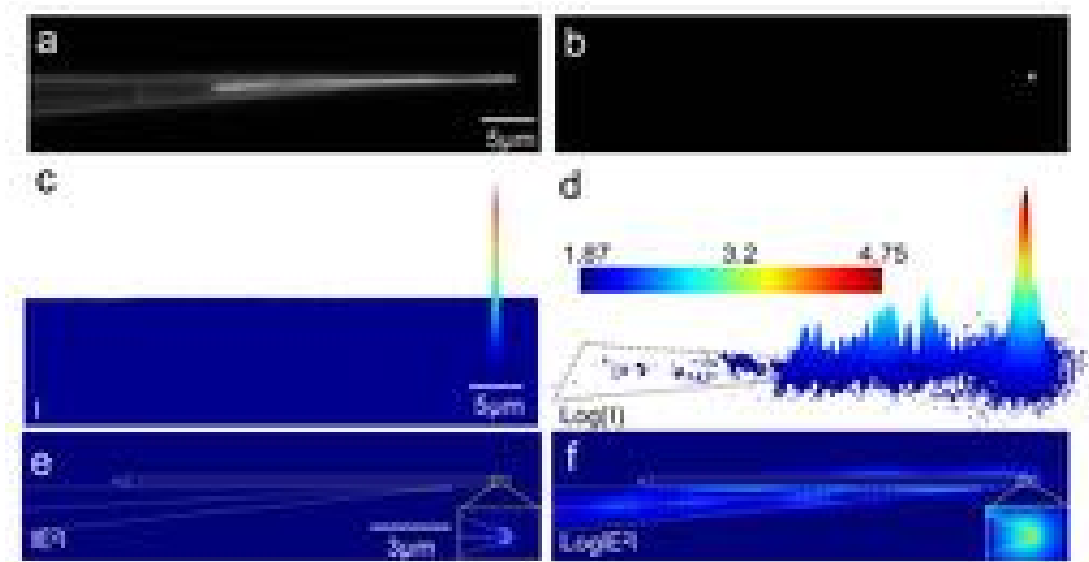
Figure S5 | High-efficiency light coupling through the AgNW-OF coupler. *(a)*, the dark-field optical microscopy image of the AgNW-OF coupler. *(b)*, the majority of the incident light sent in through the tapered fiber is coupled out to the free space through the AgNW tip. *(c)* and *(d)*, intensity profiles (in a base-10 logarithmic scale). *(e)* and *(f)*, numerical simulations confirm that the light scattered by the AgNW-OF junction is negligible. Excitation wavelength: 532nm, NW diameter: 200nm, OF taper angle: 6°.

1.4.2 Front-scattering loss

This set of experiments aims at capturing any radiative modes that scatters into the free space from the AgNW-OF coupling system. As depicted in Figure S6, a series of multi-slice images were recorded by a *high-NA optical microscope* (NA = 0.9, corresponding to ~64°), along a AgNW-OF probe. The high NA of the objective lens guarantees *(1)* the majority of the forward radiation can be collected, and *(2)* the depth of the field is small enough (~ 0.8 μm) to resolve the radiation longitudinally along the probe. A high-dynamic-range CCD camera is used to record images when the specimen focal plane moves from the AgNW tip apex towards the OF base (defined as *x* direction). The protruding length (free-standing part) of the AgNW is set to ~5 μm, and the OF tip angle to ~ 5°. This small-taper-angle optical fiber is used to stretch out the coupling process and separate the coupling regions further from each other along the *x* axis, for better multi-slice resolution.
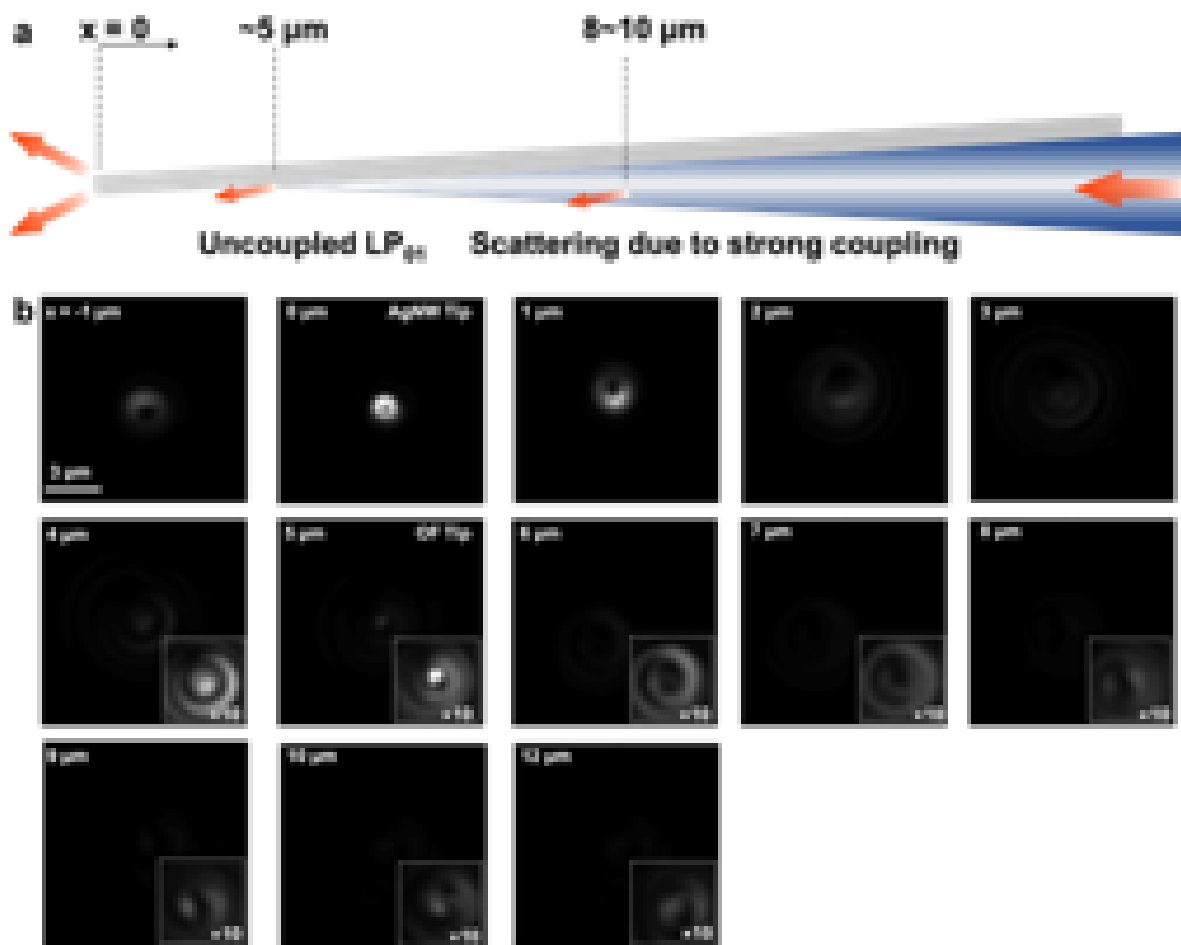
Figure S6 | Multi-slice images along a AgNW-OF probe. a, a schematic sketch of the AgNW-OF probe. AgNW diameter ~ 200nm, OF tip angle ~ 5°, and the excitation laser is 633 nm in wavelength. **b**, a series of multi-slice images, recorded by an optical microscope with a high-NA (0.9) objective lens. The insets are multiplied by 10 to increase the contrast. The intensity of the LP_{01} mode residue from the OF tip (at 5μm) and the scattered light from strong coupling zone (~ 9 μm) are about 8% and 5% of the TM_0 mode intensity at AgNW tip. All images were collected under the same conditions.

We found that the scattered light emerges mainly at three locations: the AgNW tip apex (x = 0 μm), the OF tip apex (x = ~5 μm), and the strong coupling region (x = 8~10 μm, corresponding to around 3~5 μm from the OF tip apex). At x = 0 μm (AgNW tip), a clear TM_0 pattern was observed, which gradually fades out as faint rings as the specimen focal plane moves toward the OF base. At x = 5 μm (OF tip apex), a different spot shows up clearly in focus. This

spot originates from the uncoupled LP_{01} mode remaining in the optical fiber after the coupling process. This LP_{01} residual is about 8% of the AgNW tip emission intensity. Moving further toward the OF base, this scattering spot fades into defocused rings, until another spot zooms into focus at the strong coupling zone ($x = \sim 9$ μm). The scattering at this region accounts for 5% of the AgNW tip emission intensity (TM_0 mode radiation).

2. The roles of LP_{01} mode polarization in TM_0 mode excitation

Due to the selection rule, the s-LP_{01} mode cannot excite the TM_0 mode but only the HE_1 mode. Figure S7 shows the COMSOL simulations for different excitation polarizations.
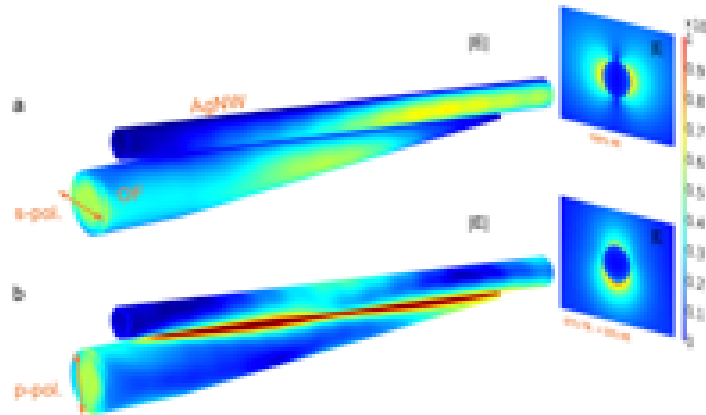
Figure S7 | Excitation of the HE1 mode using different LP_{01} modes. The electric field (|E|) on the surfaces of AgNW and OF are plotted. Insets: |E| field distribution of cross sections taken at the bottom of the AgNW. Simulation conditions: Fiber tip angle: 8 °, wavelength = 633 nm, AgNW diameter = 220 nm. The s-LP01 mode excites pure HE_1 mode, while the p-LP01 excites both TM0 and HE1 modes, at power weight of 67% and 33%, respectively.

3. The roles of TM_0 and HE_1 modes in nanofocusing

3.1 Far-field measurement

Multiple SPP modes are supported in a cylindrical waveguide. Their field distributions all

have the term $e^{im\phi}$, where ϕ is the azimuthal angle and m denotes the angular quantum number. The TM_0 mode and HE_1 mode, corresponding to m=0 and ±1 respectively, dominate the SPP excited on a AgNW with a diameter ranging from 100 nm to 300 nm. Higher order SPP modes are leaky with these diameters at the visible range. The azimuthal component is a constant in the fundamental mode (m=0), resulting in the radially symmetrical electric field profiles that are tightly bound to the nanowire and show an increasing confinement to the NW surface for a reduced NW diameter. Therefore, the TM_0 mode is particularly interesting for nanofocusing[8]. The HE_1 mode has a dipole-like mode profile and smaller fractions of field inside the metal,
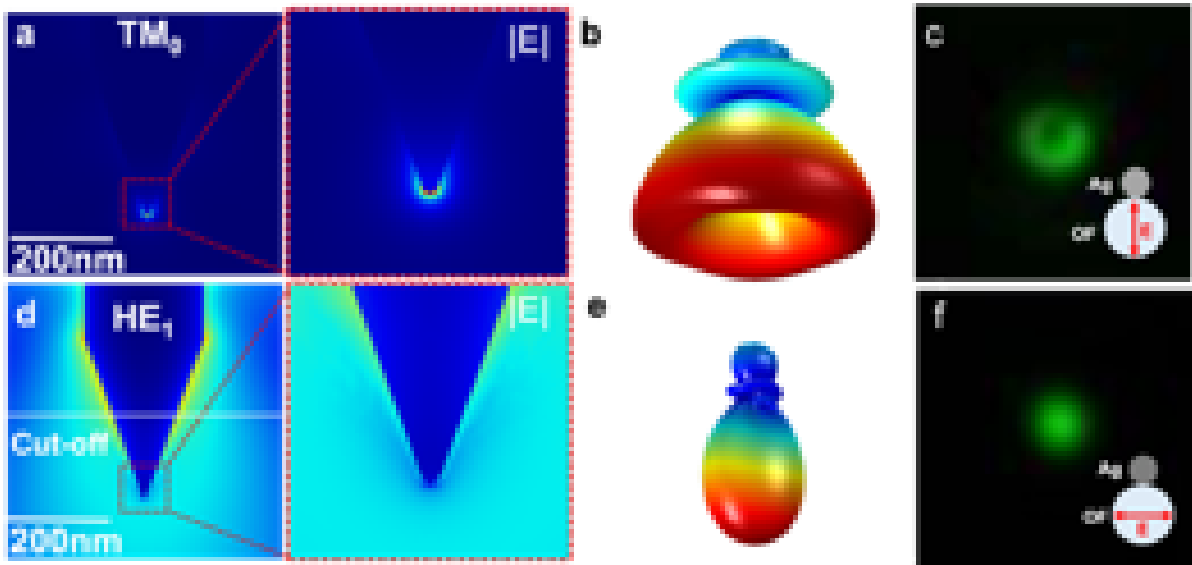
Figure S8 | Comparison of TM_0 and HE_1 mode in nanofocusing and far field radiation. *(a~c)*, TM_0 mode can form a nanoscale plasmonic hotspot at the probe apex, which generates a radially polarized ring pattern at far field. The linear polarized light along the NW placement direction in OF likely to excite the radially polarized ring pattern. *(d~f)*, HE_1 mode has a cut off at around 100nm in diameter, where it starts to couple into the free-space propagating wave. The linearly polarized light perpendicular to the direction of the NW placement in the OF is likely excite HE_1 mode and its far-field pattern is a linearly polarized Gaussian beam.

which gives less plasmonic loss and is known as the long-range SPP.

As shown in Figure 1f, the HE_1 mode has a cut-off diameter at around 100 nm for the 532 nm excitation. When the waveguide is below this cut-off diameter, the HE_1 mode index is smaller than 1 and can be coupled to the free space, or in another word, become a leaky and

unbound mode. Figure S8 shows the comparison of the two modes in nanofocusing. When the TM_0 mode propagates along the conical waveguide toward the tip apex (Figure S8a), its wavevector amplitude increases and the mode volume decreases, leading to a nanoscale plasmonic hotspot at the probe apex. The HE_1 mode in Figure S8d, however, has the wavevector amplitude decreases and eventually couples into the free space without generating a significant enhancement at the probe apex.

Their far-field radiation patterns also reflect the difference in nanofocusing. The TM_0 mode generates an enhanced electric dipole at the probe apex with the polarization along the NW axis direction. Its far-field radiation forms a radially polarized ring pattern, as shown in Figure S8b. This ring pattern was observed when the LP_{01} mode in the OF had the E-field pointing at the AgNW (Figure S8c, p-polarization). The HE_1 mode, however, has the dipole-like E-field profile and its far-field radiation is a linearly polarized Gaussian beam (Figure S8e). The HE_1 mode can be particularly excited when the E-field of the LP01 mode is s-polarized (inset of Figure S8f). The polarization of the LP_{01} mode is critical in the selective excitation. The two modes give different radiation patterns in the far-field, which can be used to calculate their power distributions.

3.2 Near-field measurement

Figure 2e is replotted in Figure S9 for further discussion. A typical SPP k-space image under 532 nm excitation, such as Figure S9a, contains three predominant features: a radially-polarized outer circle (marked as TM_0 SPP), a partially radially-polarized ring with smaller radius (marked as TM_0 +sc.), and a spot in the center (marked as HE_1+LP_{01}). The large ring is formed by the SPP at the air-gold film interface, excited by the superfocused TM_0 mode at AgNW tip apex. The central spot is the linearly-polarized HE_1 mode and the LP01 mode residue emitted from the OF tip, both of with cannot excite the 2D SPP and its radiation into the free space is attenuated by the gold film (~40 nm) before collected by the objective lens. The smaller ring represents the direct radiation of the TM_0 mode, also attenuated by the gold film. It may also contain a part of the scattered light (sc.) from the AgNW-OF coupling zone, as it has the same polarization as the *HE₁* mode and cannot be fully removed in Figure S9b. From these figures, we estimate that the HE_1 mode and the scattered light weight ~15% of the total intensity, and the other 85% is contributed by the TM_0 mode. Under the 633nm excitation, since the gold film is more reflective to the free-space light and less lossy to the SPP, the k-space image quality is drastically improved, as shown in Figure S9b. The HE_1 mode and the scattered mode in the center of the pattern weigh only 7% of the total intensity.
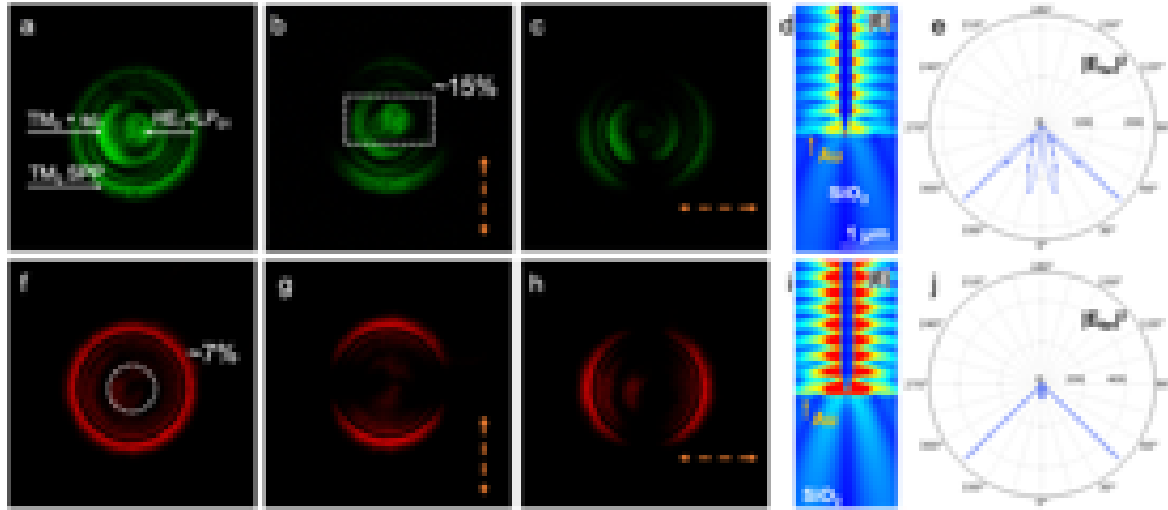
Figure S9 | Improved k-space measurement and TM_0 mode analysis. a~c, the polarization-resolved k-space images with 532 nm excitation. **d**, E-field distribution with a TM_0- mode excitation launched at the AgNW butt reveals that there is a strong radiation inside glass, directly from the AgNW tip apex, even after the attenuation of the gold film (40 nm in thickness). **e**, far-field radiation pattern of the wave in glass. **f~j** are experiments and simulations similar to a~e, but conducted by 633 nm excitation. In **f**, the central part circled by the dashed ring has the intensity ~7% of the total.

To understand the directly transmitted TM_0 mode (small rings), further analysis was conducted through COMSOL simulation. As shown in Figure S9d and i, when a pure TM_0 mode is launched onto the AgNW from the top, the superfocused TM_0 mode at the AgNW tip apex not only excites propagating SPP mode at the air-gold interface (not shown here), but also excites EM wave that transmits directly through the ultra-thin gold film (40 nm in thickness, after optimization to the SPP intensity), leaving two clear trajectories in the underlying glass substrate. As a result, in the *k*-space measurement, the TM_0 mode induces not only outer rings corresponding to the propagating SPPs, but also a series of concentric rings with smaller *k*, which were observed both in the experiments (Figure S9a and f) and far-field simulations (Figure S9e and j).

4. External nanofocusing efficiency η_{ex}

The external nanofocusing efficiency (η_{ex}), defined as the percentage of the input fiber power that can be delivered to the AgNW tip apex, is determined by two factors: the coupling efficiency of the AgNW-OF junction (η_c) and the nanofocusing efficiency of the sharp-tip AgNW (η_{nf}), through a simple equation:

$$\eta_{ex} = \eta_c \times \eta_{nf} \qquad\qquad S(4)$$

4.1 Coupling efficiency η_c measurement

In order to measure the coupling efficiency, we need to consider the LP_{01} mode power in the optical fiber, the radiated TM_0 mode from the AgNW tip, the radiation efficiency of the tip and the collection efficiency of the measurement.

LP_{01} mode power measurement: We used the far-field radiation intensity radiated from a tapered optical fiber tip and collected by a CCD (16 bits) to estimate the light intensity of the LP_{01} mode in the optical fiber. This estimation is valid due to the low reflection coefficient and directional radiation from the tapered optical fiber tip. As shown in Figure S10, the effective mode index of a silica waveguide slowly decreases towards the tip apex. This process is adiabatic since the taper angle is small (~6 to 10°) and the wavevector decreases slowly along the propagation direction. As a result, the optical reflection induced by this adiabatic process is negligible. By integrating the Poynting flux at the input port, the reflection efficiency is found around 1.3×10^{-4} (taper angle 6°, light wavelength 532 nm).

The low back reflection efficiency also benefits from the high-efficiency coupling from the LP_{01} mode to the free space mode at the phase matching region, with optical fiber diameter around 100~150 nm where the effective index of the LP_{01} mode is reduced to 1. The far-field radiation pattern (Figure S10c and d) has a small radiation angle since the large-angle scattering at the phase-matching region is weak. The collection efficiency through a high NA (NA=0.9) lens is near unity (T= 99.991%). Therefore, the light intensity collected by the high-dynamic-range CCD can be used to represent the LP_{01} mode power.

It is worth noting that the transmission efficiency of the lens itself is not important in this calculation as it also affects the intensity of the AgNW radiation and will cancel out in the final equation.
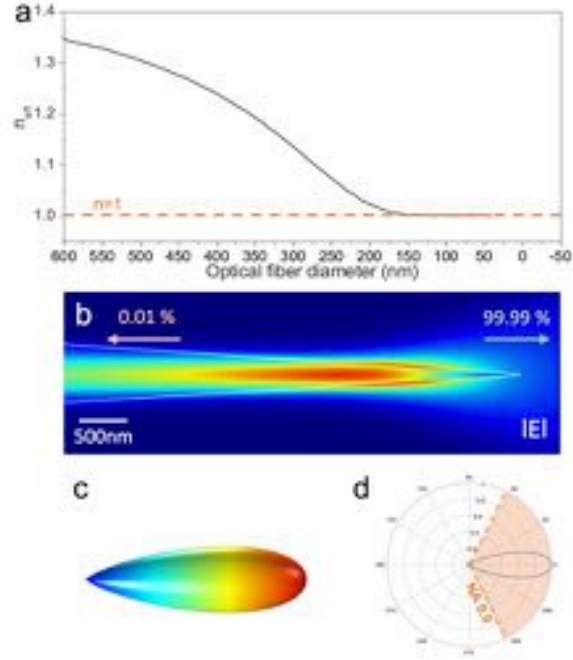
Figure S10 | Transmittance of a tapered optical fiber and its far-field radiation pattern. **a**, Calculated effective mode index (n_{eff}) of LP01 in an optical fiber waveguide with different fiber diameters. **b**, E-field distribution in the tapered optical fiber. (**c-d**), 3-D and 2-D far-field radiation patterns of the light from a tapered optical fiber (8° tip angle) that show a small radiation angle. The simulation results were acquitted with COMSOL Multiphysics. The wavelength of light and the taper angle of the optical fiber are 532 nm and 8° respectively. The collection efficiency of the far-field radiation pattern by a high NA (0.9) objective lens is 99.991%.

Coupling efficiency calculation: As shown in Figure S11, the coupling efficiency η_c refers to the percentage of the input power in the OF (P_{in}) that can be coupled into the TM_0 mode (P_{TM0}):

$$\eta_c = P_{TM0}/P_{in} \qquad\qquad S(5)$$

Besides of P_{TM0}, other channels that consume the input power are the plasmonic/scattering loss during the coupling process (P_{loss}), and the HE_1 mode power (P_{HE1}) that cannot be used for nanofocusing. To measure P_{in} and P_{TM0}, we carried out the experiment depicted in Figure S11a and b. P_{in} was measured by imaging the radiation pattern from a bare tapered OF directly. Unlike a flat OF terminal facet prepared by the standard cleaving method, the tapered OF has a gradual and continuous change in the effective mode index (momentum),
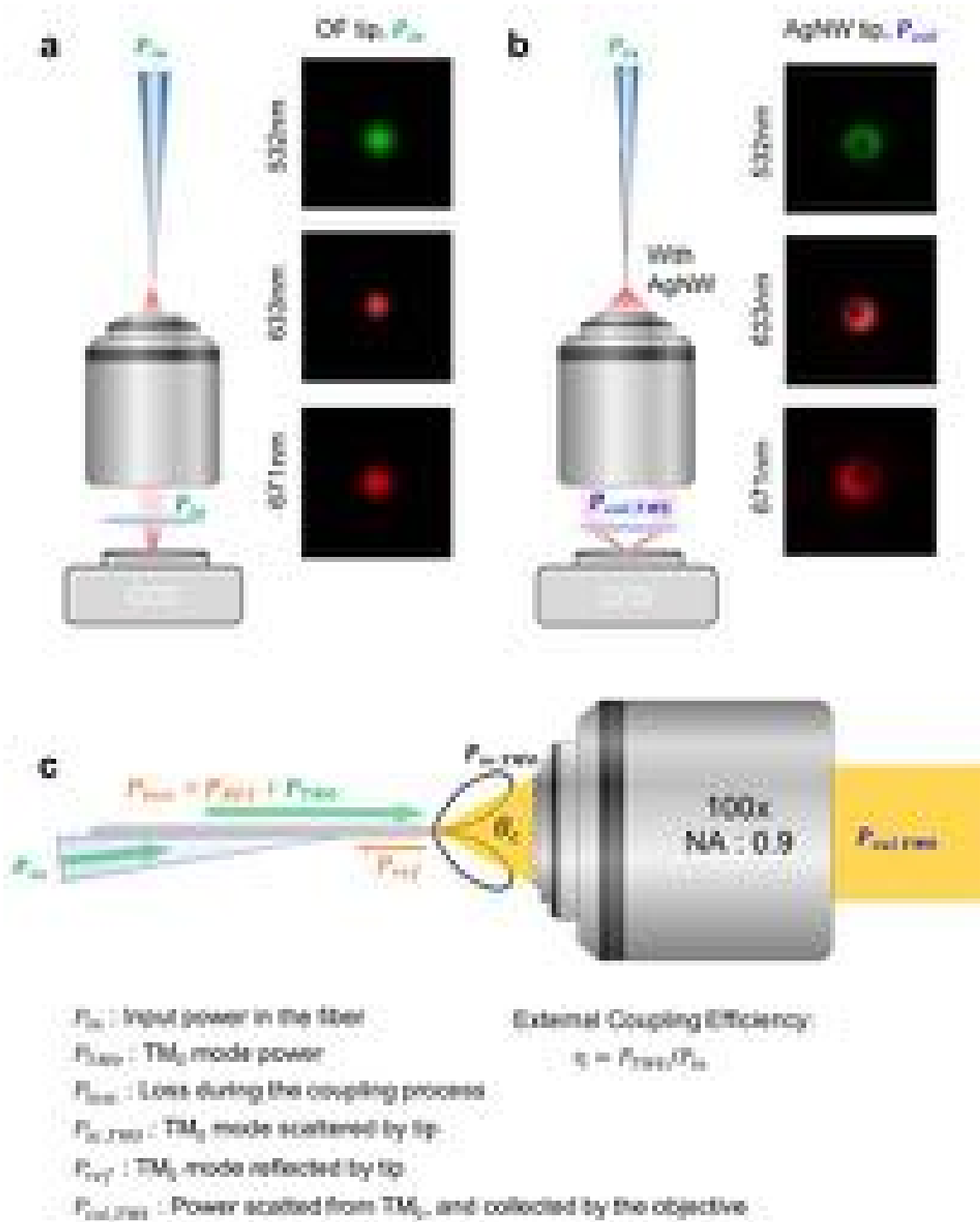
18

Figure S11 | AgNW-OF coupling efficiency (η_c) measurement. *(a)*, Laser spots at the tip of a bare tapered OF. ***(b)*,** Images of the AgNW tip, with the same input power (P_{in}). The TM_0 mode weight can be determined from the k-space measurement. ***(c)*,** η_c can be determined after considering the tip radiation efficiency and system collection efficiency.

which reduces the reflection to almost zero. Moreover, the radiation angle of the tapered OF is ~12°, which can be fully collected by the objective lens (NA=0.9). Therefore, P_{in} recorded by the CCD camera can be used to represent the optical power in the fiber.

P_{TM0} can be calculated from the optical power radiated from the AgNW tip and collected by the microscope (named $P_{col,TM0}$), after considering the radiation efficiency $(P_{sc,TM0}/P_{TM0})$ and the collection efficiency $(P_{col,TM0}/P_{sc,TM0})$. The coupling efficiency η_c can be written as:

$$\eta_c = \frac{P_{TM0}}{P_{in}} = \frac{P_{col,TM0}}{P_{in}} / \left(\frac{P_{col,TM0}}{P_{sc,TM0}} \cdot \frac{P_{sc,TM0}}{P_{TM0}} \right) \qquad\qquad S(6)$$

The ratio of the measured TM$_0$ output power to the input power $\left(\frac{P_{col,TM0}}{P_{in}} \right)$ was 25% for 532nm, 41% for 633nm, and 38% for 671nm. The corresponding total collection efficiencies $\left(\frac{P_{col,TM0}}{P_{sc,TM0}} \cdot \frac{P_{sc,TM0}}{P_{TM0}} \right)$ are 63%, 56% and 58%, for the sharp-tip AgNW (tip angle ~40°) used in the measurement. Consequently, the coupling efficiencies η_c are 40%, 72%, and 66%, for 532nm, 633nm, and 671nm, respectively. It is worth noting that by normalizing $P_{col,TM0}$ with P_{in}, the influences from the equipment can be canceled, such as the transmittance of the objective lens and the quantum efficiency of the CCD camera.

4.2. Nanofocusing efficiency η_{nf} of sharp-tip AgNWs

As theoretically proposed by Pile and Gramotnev[9], symmetric SPP modes (with respect to the charge distribution across the waveguide) propagating towards the tip of the wedge/groove/edge can have both the phase and group velocity reduce towards zero. Unlike the HE$_1$ mode, the TM$_0$ mode has axisymmetric E-field and charge distribution and can potentially be adiabatically focused to the probe apex.

However, the adiabatic approximation for high-efficiency nanofocusing requires the insignificant variation of the wave number of the propagating plasmon along the propagation direction:

$$\left| d(k_z^{-1}) \big/ dz \right| \ll 1$$

where k_z is the z component of the real part of the wave vector of the TM$_0$ mode plasmon. To satisfy this requirement, the tip angles in the reported works mostly fall in the range of 2~6° [10].
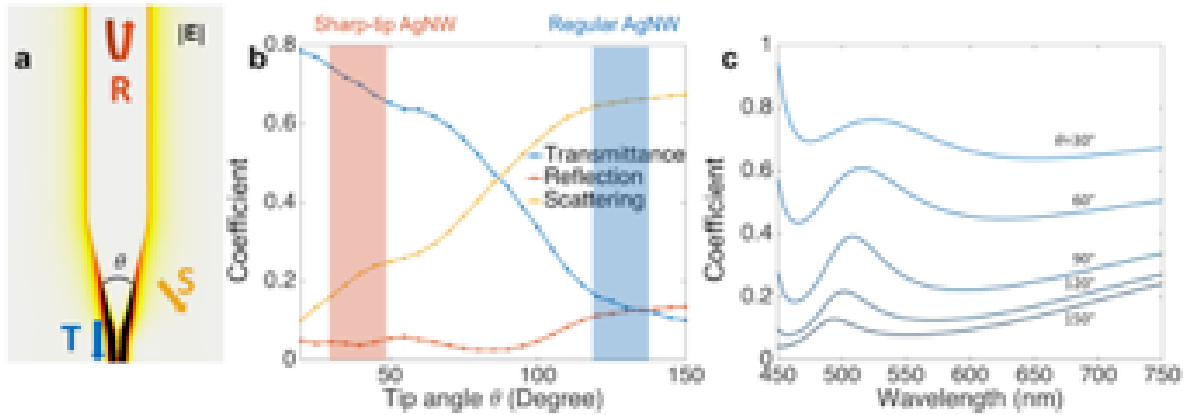
Figure S12 | Nanofocusing efficiency of a AgNW tip. *(a)*, Sketch of the nanofocusing model. The energy dissipation channels (including transmittance, scattering and reflection) are illustrated. *(b)*, The coefficients dependence on tip angles. *(c)*, The wavelength-dependence of the coefficient.

The chemically etched AgNWs have sharp ends with tip angles between 30~50°, leading to a relatively fast changing rate of k_z and consequently, large scattering loss compared with the adiabatic nanofocusing. Here, we use the FEA method (COMSOL Multiphysics) to evaluate the scattering loss during the nanofocusing process. The model used in the simulation to mimic the tapered AgNW tip is a tapered mode coupler (with tip angle θ) connecting the AgNW waveguide (200nm in diameter) with a narrow Ag waveguide (10nm-in-diameter), as shown in Figure S12a. The transmittance, scattering loss and reflection ratio of a TM$_0$ mode launched on the AgNW are plotted in Figure S12b. Compared with regular AgNWs with tip angle of around 120°, the sharp-tip AgNWs (θ between 30~50°) increase the transmittance (nanofocusing efficiency) of 532nm excitation from ~10% to ~70%.

The overall external nanofocusing efficiency η_{ex} from the OF mode to the AgNW tip apex is thus the product of the fiber-to-AgNW external coupling efficiency (~70%) and the nanofocusing efficiency (~70%), which is about 50%.

4.3. Fiber-In Fiber-Out (FIFO) loss

The theoretical and experimental demonstrations of the high-efficiency selective coupling propose that a fiber-in fiber-out configuration can be used for near-field optical characterizations. In order to demonstrate its feasibility, we measured the transmission of two tapered OFs that are connected via a AgNW, which reflects the overall coupling efficiency of FIFO configuration.

Figure S13 shows the experiment to measure the FIFO efficiency. Two identical tapered OFs (OF1 and OF2) were aligned parallel and placed tip to tip, leaving a 25 µm gap in between. The incident light (532nm) sent in bare OF1 was firstly measured by an optical powermeter (PM320E with S120C photodiode sensor, Thorlabs). When the input power was 35 µW in OF1, the output power from OF2 (without AgNW) was around 0.2 µW. This light originated from the direct coupling of two bare tapered fibers and was subtracted from future measurements. In the second measurement shown in Figure S13b, a AgNW with a diameter of ~200nm was firstly mounted onto OF2, which was then used as a handle to mount the other end of the AgNW to OF1. The output power from OF2 (with the AgNW) increased to 2.5 µW. Therefore, the total transmittance is 6.5% (-11.8dB). After deducting the plasmonic loss on the AgNW waveguide (0.3 dB/µm × 25 µm = 7.5 dB)[3], the two AgNW-OF couplers each contribute ~-2.2dB optical loss, which corresponds to ~60% in transmittance. This result is higher than the direct measurement result in **Figure** 5 (~40%), which may due to the contribution of HE_1 mode that has longer propagation length.
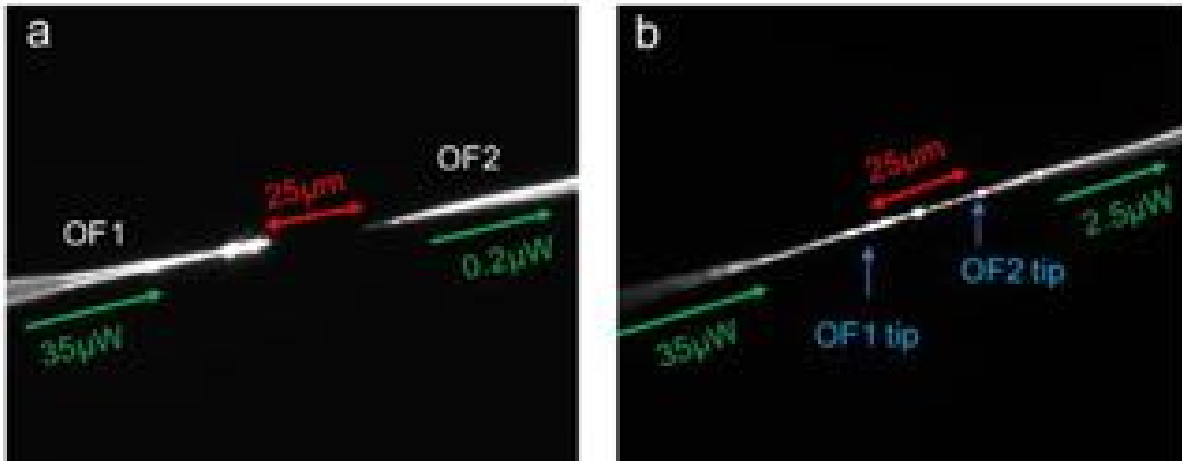
Figure S13 | Overall coupling efficiency of Fiber-In and Fiber-Out (FIFO) configuration. The light coupling occurs in the route of conversion of the photon in a tapered OF1 to SPP in AgNW and the conversion of the SPP back to photon in the other OF2. *(a),* Measurement of direct light coupling (without AgNW) from a tapered OF to the other one 25µm distant from each other. *(b).* Measurement of photon coming out of the OF2 end that has been converted from photon to SPP and SPP to photon at the two light coupling regions at the two OF tips. The NW diameter and wavelength of the laser are ~200 nm and 532nm respectively.

5. TM₀-mode-enhanced fluorescent radiation analysis

In this simulation, we use a classical oscillating electric dipole $\boldsymbol{p}$ placed close to the AgNW tip apex to calculate the radiation enhancement, to examine the role of the TM_0 mode in the radiation process. This theoretical treatment has been proven to be an excellent model in both theoretical and experimental reports[11-13]. As shown in Figure S14, the total energy transfer rate Γ_{tot} from an electric dipole place at the vicinity of probe apex can be considered as the sum of the nonradiative rate Γ_{nr} and the radiative rate Γ_r. The nonradiative channel Γ_{nr} mainly accounts for the ohmic loss in the AgNW and the metallic substrate, and a small portion of high-wavenumber SPP that cannot be conducted either by the AgNW waveguide or the metal surface. The radiative channel Γ_r includes three parts: the radiation into the 1D-SPP along the AgNW (Γ_{AgNW}, mainly in TM_0 mode), the 2D-SPP along the metal substrate (Γ_{sub}), and the direct coupling into the scattered light in free space (Γ_{sc}), which can be written as:

$$\Gamma_{tot} = \Gamma_r + \Gamma_{nr}$$

$$\Gamma_r = \Gamma_{AgNW} + \Gamma_{sub} + \Gamma_{sc}$$

In conventional TERS instruments with side-illumination and collection, the Γ_{sc} channel is utilized for the signal detection. The drawbacks of this method are the limited ratio of Γ_{sc} over Γ_r, and the implicitly limited numerical aperture (NA) for detection. To improve the collection efficiency, parabolic mirrors have been introduced[14], where the optical alignment is challenging. The radiation channel along the metallic probe in the form of SPP, here marked as Γ_{AgNW}, has been overlooked due to the difficulty in coupling them back into the far-field propagating waves. Although theoretical research has pointed out the importance of this radiation channel[12], to the best of our knowledge, it has not been used for radiation signal detection before. These high-wavenumber SPP modes that eventually dissipate into heat are generally considered as a major contribution to the quenching effect[15].

Figure S14 shows the contributions of each radiative channel, with the numbers outlined in Table S1. Two configurations are considered here: AgNW-dipole-dielectric substrate configuration (Regular) and AgNW-dipole-metal substrate configuration (gap mode). The first one is to mimic near-field imaging techniques including scattering-NSOM and near-field photoluminescence imaging, and the second one is to imitate the TERS measurement. We find that in both cases, the 1D-SPP channel along the AgNW dominates the radiative decay, which may due to the fact that the high-wavenumber SPP modes near the probe apex have a

significantly higher local density of state (LDOS) than the free-space propagating wave mode does. A large portion of the radiation energy is thus dumped into the SPP modes along the AgNW, which can be utilized for near-field imaging with improved signal-to-noise ratios.
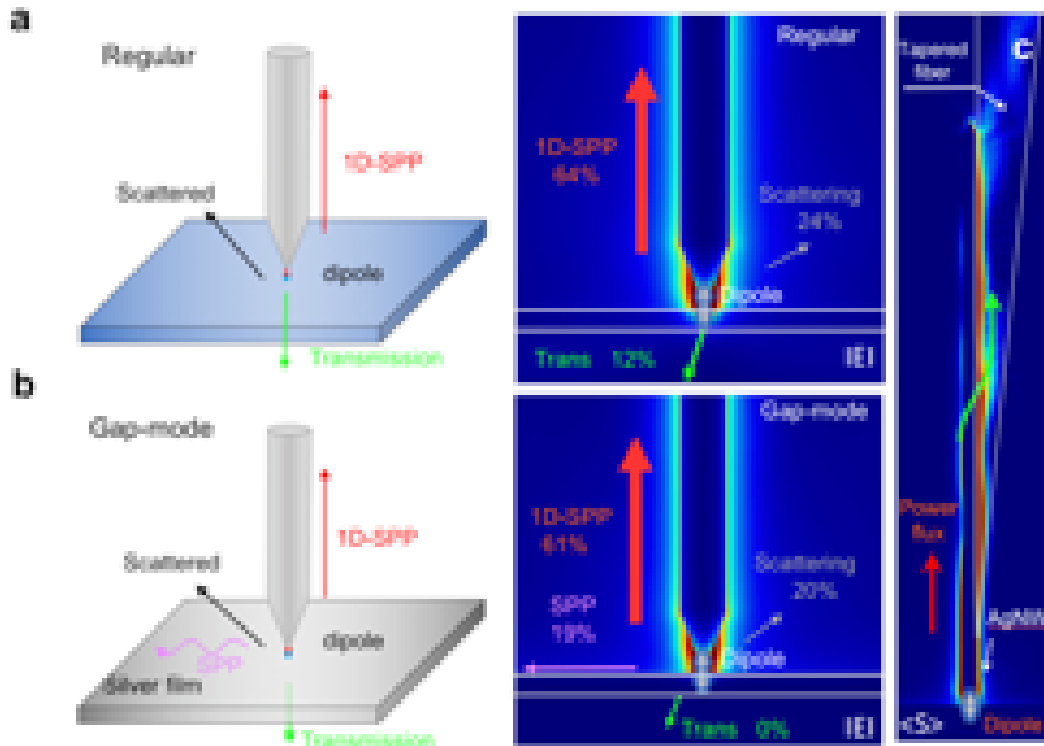

Figure S14 | Schematic for understanding the radiation channels in a modified emission system. *(a)*, An electric dipole is placed between a dielectric substrate and a sharp-tip AgNW, with its polarization normal to the substrate. Full-wave simulation on the right shows the contribution of each radiative channel to the total radiative energy transfer (Γ_r). *(b)*, The dipole is placed between the AgNW and a silver substrate. *(c)*, The Poynting flux image shows that the 1D-SPP on the AgNW is back-coupled to the OF, as suggested in Figure 1 in the paper. Simulation parameters for all configurations: AgNW diameter is 200 nm, tip radius is 5 nm, the dipole oscillation frequency corresponds to 532 nm wavelength in free space, AgNW-to-substrate distance is 1 nm.

Table S1 Contribution from each radiative channel

Configuration	Γ_r/Γ_{tot}	$\Gamma_{AgNW}/\Gamma_{tot}$	Γ_{sc}/Γ_{tot}	$\Gamma_{SPP}/\Gamma_{tot}$
Regular	81%	63%	5.4%	NA
Gap-mode	92%	66%	19%	7%

6. STM measurement

6.1. Probe preparation

Tapered OF: In order to achieve a high coupling efficiency from OF to AgNW, the end of the OF must be tapered smoothly and uniformly. Chemical wet etching technique can taper OF with a high quality of sharpness and smoothness and have been commonly used for near-field optical probes.[16,17] Here, the jacket at the fiber end (Thorlabs, model S405-XP) was cleaved and sonicated in acetone and DI water to remove residues form the surface of the cladding layer. The cleaved fiber end was then immersed in 48% hydrofluoric acid (HF, Sigma-Aldrich) covered with isooctane (≥99%, Fisher-Scientific). The fiber was pulled out of the HF using a syringe pump at a different pulling speed to control the taper angle. The fiber was then washed with DI water thoroughly.

Mechanical vibration in STM probe: Vibrational motion of our AgNW-OF probe due to the external perturbation limits the spatial resolution of both STM and Raman images. Therefore, the vibrational displacement of our waveguide driven by external perturbation must be considered. For our AgNW-OF probe, the protruding length of AgNW from the OF tip is around 1~2 μm. Compared with the OF (~100 μm for the conical region), the displacement of the NW is negligible. Consequently, FEA modeling (COMSOL Multiphysics) was conducted to calculate the relative displacement of the OF as a function of the taper angle when driven by a vertical force (Figure S15). The result shows that a significant reduction of the displacement was obtained with a taper angle larger than 6°. Considering the range of the taper angle for the efficient excitation of TM$_0$ mode discussed in the session S1 together with the mechanical vibration, the optical fibers with taper angles ranging from 6° ~ 10° were used for the STM scanning in this work.
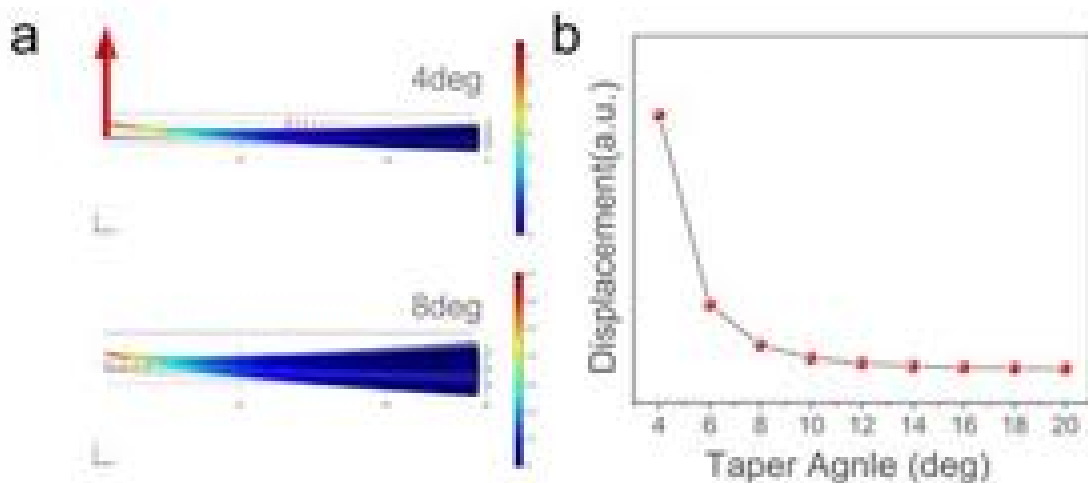
Figure S15 | Simulated displacement of OF with different taper angles. *(a),* Displacement distribution along the OF with 4 and 8 taper angles. The arrow represents the displace gradient. *(b),* Relative displacement as function of OF taper angle with a certain shear force applied along the OF.

AgNWs: AgNWs longer than 100 μm with diverse thickness were synthesized via polyol-mediated reduction of AgNO₃ employing polyvinylpyrrolidone (PVP) to guide one dimensional growth[18]. It is known that the oxidative etching occurs during synthesis and storage, resulting in rounded AgNW tips. In this work, the tip shape of the AgNW must be considered as it determines the nanofocusing efficiency and the spatial resolution in TERS imaging. Accordingly, all AgNWs in this work were synthesized and purified in the deoxygenated solution. 5ml ethylene glycol in a pear-shaped flask was immersed in a silicone oil bath at 152 °C under stirring (400rpm), and the flask was purged with nitrogen. While the flask is heated up, 6ml AgNO₃ (0.094M, 99+%, Fisher) and 6ml PVP (0.147 M, avg Mw # 55 000, Sigma-Aldrich) in ethylene glycol (EG, 99%, Fisher) were prepared. After the EG in the pear-shaped flask had been heated and purged for 30mins, 80μl CuCl₂(4mM, 99.995%, Sigma-Aldrich) was added, and the flask was purged for an additional 15 minutes. The 3ml PVP solution was injected, along with the AgNO₃ solution at the injection speed of 125 μl/min using two syringe pumps[19]. After 40mins of the injection, the reaction was stopped by removing the flask from the silicon oil bath. After cooling for 15 minutes at room temperature, the AgNWs were purified with deoxygenated
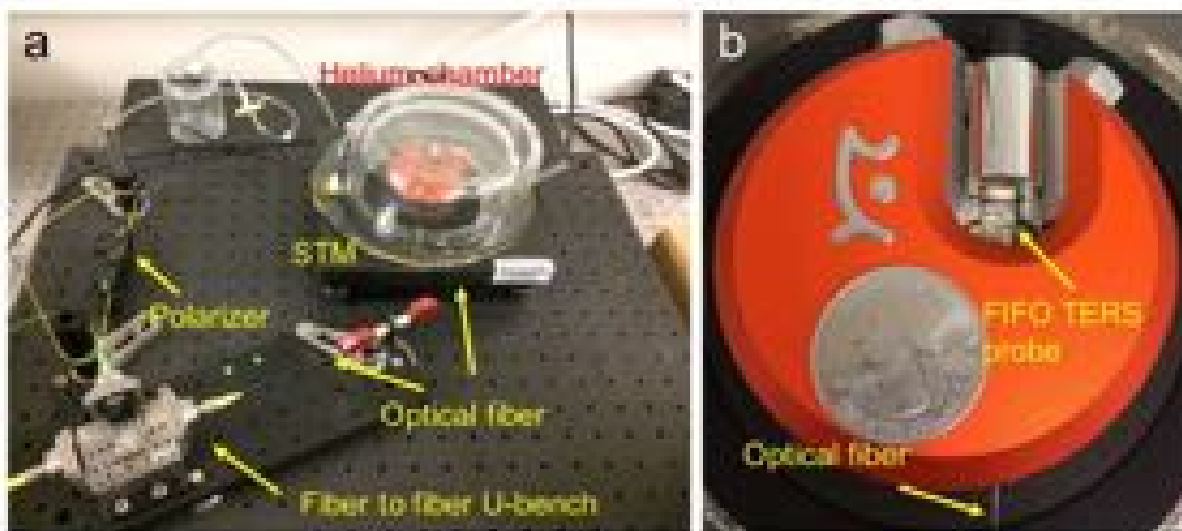
Figure S16. *(a-b),* The FIFO STM-TERS system. A fiber bench system (U-bench) is used to realize the FIFO configuration. The FIFO TERS probe was then integrated with a compact ambient STM (NaioSTM by Nanosurf).

ethanol by centrifugation at 800 RPM for 20 minutes at least 5 times. The sharp-tip AgNWs were prepared through a similar method, as detailed in Ref. 20. The synthesized AgNWs have tip angles around 30~50°.

STM probe preparation: In order to reduce the mechanical vibration of the OF, the tapered fiber used for the STM scanning was etched through two steps for different taper angles. In the first step, the fiber was etched without being pulled by a syringe pump. Therefore, a large taper angle was achieved. When the etching process is close to the end, we ran the syringe pump to pull out the OF from the HF solution for the reduction of the taper angle. The fiber is then thoroughly rinsed with DI water, and the tip region (~ 30μm) was coated with nail polish. After it was dry, 70 ~100 nm Au was deposited on the fiber through an E-beam evaporator at room temperature with 0.5~1Å/s depositing rate. The nail polish at the tip of the OFs was removed by immersing into acetone with gentle sonication and washed with DI water for multiple times. The tapered fiber was then glued onto a short tungsten needle, which has a large mechanical stiffness and is used as a supporter for the fiber. The Au electrode on the OF was then electrically connected with the tungsten needle using silver paste. The tungsten needle was used to hold the fiber in the STM piezoelectric holder in Nanosurf as shown in Figure S16b.

6.2. Experiment setup

Our STM-TERS system is composed of a 2-paddle polarization controller, a fiber to fiber U-bench, and the STM in a Helium chamber as shown in Figure S16a. Using the 2-paddle polarization controller, the incident light was polarized in the direction toward the AgNW to excite TM_0 mode. The fiber-to-fiber U-bench consists of a reflecting mirror, (4% reflection of incident light and 96% transmission of the spectrum range of Raman signals) and a long-pass edge filter (>533nm) as shown in Figure 3. The STM is covered with double glasses, and the inside was filled with Helium gas. This double-glass Helium chamber can reduce the acoustic noises by ~ 70 dB and increase heat dissipation to improve imaging quality and prevent heat damage to the probe and sample.

6.3. TERS sample preparation

Monolayer 4-Amonithiophenol (4-ATP): 100nm Au was deposited on a cover glass using E-beam evaporator at room temperature with 0.5~1Å/s deposition rate. The Au film was then incubated in 1mM 4-ATP (97%, Sigma-Aldrich) ethanol solution for 12h and then thoroughly rinsed with ethanol.

Monolayer Rhodamine 6G (R6G): Au substrates were prepared in the same manner as for 4-ATP monolayer. The R6G monolayer was prepared following the described procedure in Ref 21. The samples were prepared by incubating the Au films in the R6G dye molecule solutions ($3×10^{-4}$M, 99%, Sigma Aldrich) for 6h. The gold film was then rinsed with ethanol thoroughly to achieve monolayer coverage.

SWCNTs/Au: 100nm Au was deposited on a freshly exfoliated mica layer with a 0.5~1Å/s deposition rate using E-beam evaporator at room temperature. The Au/mica layer was then annealed at 350C° for 1hr to achieve the rearrangement of Au. The subsequent gradual decrease of the temperature enables the crystallization of Au into a minimum-energy configuration {111} facet. Finally, the Au film was glued with epoxy to a glass substrate, and it was mechanically peeled off. Single wall carbon nanotubes (conductive aqueous ink, purchased from Sigma-Aldrich) were sprayed on the Au film on a hot plate at 60°. The SWCNTs/Au was gently immersed in DI water and placed in an oven at 80°C for 1hr to remove surfactants on the surface of SWCNTs. After cooling it down to room temperature, the water was refreshed by the continuous flow of DI water. Finally, the SWCNTs/Au was dried by blowing gently with a nitrogen gun.

6.4. TERS result analysis

Maximum count per second (CPS) of TERS R6G

We examined the TERS performance of the FIFO nanoscopy using R6G, which is commonly used for the demonstration of single molecule detection due to its large resonance Raman cross-sections[22]. TERS spectra were acquired at different points with a 532nm laser (1μW in fiber) with the AgNW tip tunneling current set at 2nA (Figure S17). Although the vibrational modes of R6G observed here have some discrepancies with the typical characteristic peaks due to different charge transfer, local field distribution, and field-gradient in the gap, the Raman peaks here are in the vibrational motion category that has been calculated or observed experimentally: sharp signals at around 1250 cm^{-1}, assigned to C-O-C stretching mode, 1500 cm^{-1}, assigned to aromatic C-C stretching mode, and other minor peaks at 1009 cm^{-1}, 1143 cm^{-1}, 1183 cm^{-1}, and 1201 cm^{-1}, which is associated with different observable vibrational motions.[23-26] The count per second(cps) of the Raman intensity acquired with our AgNW/OF TERS probe
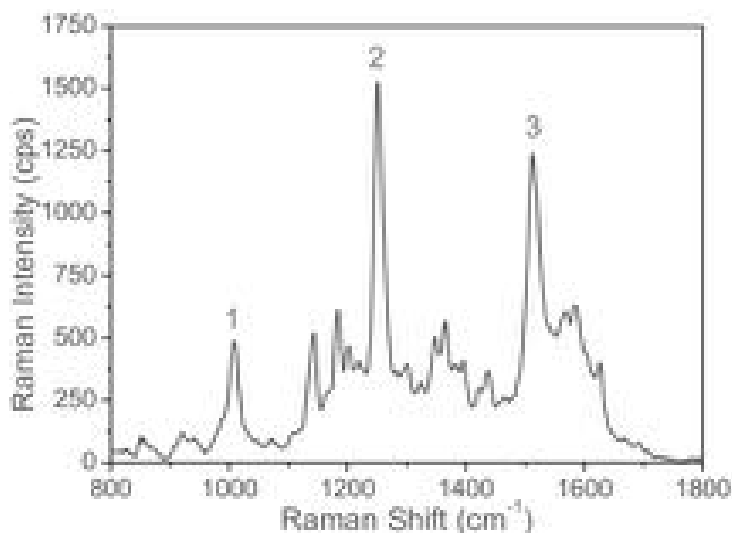
1) Phenyl ring with the COOC$_2$H$_5$ group or a pair of methyl group adjacent to the xanthene ring or xanthene ring
2) C-O-C stretching
3) Aromatic C-C stretching

Figure S17 | Raman spectra of R6G obtained with FIFO configuration and the assignment of the representative peaks.

with FIFO configuration can be as high as ~1520cps, which, to the best of our knowledge, is the highest Raman signal intensity obtainable with TERS. This may due to the efficient collection channel (1D-SPP) as discussed in Section 5.

Analysis of SWCNTs peaks acquired with FIFO STM-TERS.

Figure S18 compares the Raman spectra of SWCNTs obtained with conventional Raman spectroscopy with one of our STM-TERS probe with FIFO configuration. The peaks observed with STM-TERS are slightly different from the conventional Raman spectra of SWCNTs. It shows that the G$^-$ and G$^+$ bands (doubly degenerate phonon modes: TO and LO) were shifted and separated from each other. The separation can be understood in the way that the torsional strain induced by the AgNW tip upshifts only the G$^+$ bands toward a higher frequency due to change of the C-C bond lengths in the circumferential direction.[27] On the other hand, the slight downshift of the G$^-$ band mainly originates from the small diameter of the scanned SWCNTs and the shift can be enhanced further due to the slight uniaxial strain which can occur together with the torsional strain.[28,29] Dynamic temperature variation, together with tightly localization of optical field with a nanoscale cavity at the apex of the AgNW tip may also lead to the further shift of both peaks.[28,30] New peak originating from the splitting of the G$^-$ band was also observable due to the broken symmetry attributed by the torsional strain.[31] These peaks were not from the surfactants (sodium dodecyl sulfate, SDS) used for the dispersion of the SWCNTs, since the
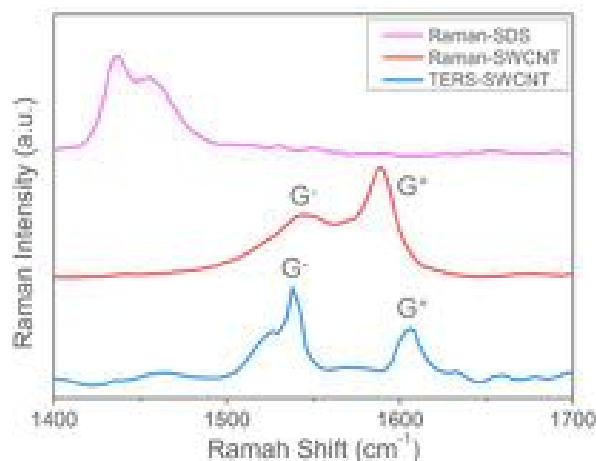

Figure S18 | Comparison of SWCNT Raman spectra obtained with STM-TERS and conventional Raman apparatus.

samples were thoroughly washed with both hot and cool DI water after being spread on Au film. Moreover, the Raman spectra of SDS show no peaks in the spectrum range of 1500–1700cm^{-1} but strong Raman peaks at 1400-1460cm^{-1}, which are assigned for CH_2 bending modes[32].

7. References

1   Chuang, S.L. *Physics of Optoelectronic Devices*.   (Wiley, 1995).

2   Zhang, S. *et al.* Chiral Surface Plasmon Polaritons on Metallic Nanowires. *Phys. Rev. Lett.* **107**, 096801, (2011).

3   Kim, S., Bailey, S., Liu, M. & Yan, R. Decoupling co-existing surface plasmon polariton (SPP) modes in a nanowire plasmonic waveguide for quantitative mode analysis. *Nano Res.* **10**, 2395-2404, (2017).

4   Paspalakis, E. Adiabatic three-waveguide directional coupler. *Opt. Commun.* **258**, 30-34, (2006).

5   Ciret, C., Coda, V., Rangelov, A.A., Neshev, D.N. & Montemezzani, G. Broadband adiabatic light transfer in optically induced waveguide arrays. *Physical Review A* **87**, 013806, (2013).

6   Johnson, P.B. & Christy, R.W. Optical Constants of the Noble Metals. *Phys. Rev. B* **6**, 4370-4379, (1972).

7   Lan, T.-H. & Tien, C.-H. Study on focusing mechanism of radial polarization with immersion objective. *Jpn. J. Appl. Phys.* **47**, 5806, (2008).

8   Gramotnev, D.K. & Bozhevolnyi, S.I. Nanofocusing of electromagnetic radiation. *Nat. Photon.* **8**, 13, (2014).

9   Vernon, K.C., Gramotnev, D.K. & Pile, D.F. Adiabatic nanofocusing of plasmons by a sharp metal wedge on a dielectric substrate. *J. Appl. Phys.* **101**, 104312, (2007).

10   Stockman, M.I. Nanofocusing of optical energy in tapered plasmonic waveguides. *Phys. Rev. Lett.* **93**, 137404, (2004).

11   Barnes, W.L. Fluorescence near interfaces: the role of photonic mode density. *J. Mod. Opt.* **45**, 661-699, (1998).

12   Issa, N.A. & Guckenberger, R. Fluorescence near metal tips: The roles of energy transfer and surface plasmon polaritons. *Opt. Express* **15**, 12131-12144, (2007).

13   Qian, H. *et al.* Efficient light generation from enhanced inelastic electron tunnelling. *Nat. Photon.* **12**, 485-488, (2018).

14   Stanciu, C., Sackrow, M. & Meixner, A.J. High NA particle- and tip-enhanced nanoscale Raman spectroscopy with a parabolic-mirror microscope. *J. Microsc.* **229**, 247-253, (2008).

15   Pelton, M. Modified spontaneous emission in nanophotonic structures. *Nat. Photon.* **9**, 427-435, (2015).

16   Stöckle, R. *et al.* High-quality near-field optical probes by tube etching. *Appl. Phys. Lett.* **75**, 160-162, (1999).

17   Lambelet, P., Sayah, A., Pfeffer, M., Philipona, C. & Marquis-Weible, F. Chemically

etched fiber tips for near-field optical microscopy: a process for smoother tips. *Appl. Opt.* **37**, 7289-7292, (1998).

18   Sun, Y., Yin, Y., Mayers, B.T., Herricks, T. & Xia, Y. Uniform silver nanowires synthesis by reducing AgNO3 with ethylene glycol in the presence of seeds and poly (vinyl pyrrolidone). *Chem. Mater.* **14**, 4736-4745, (2002).

19   Korte, K.E., Skrabalak, S.E. & Xia, Y. Rapid synthesis of silver nanowires through a CuCl- or CuCl2-mediated polyol process. *J. Mater. Chem.* **18**, 437-441, (2008).

20   Ma, X. *et al.* Sharp-Tip Silver Nanowires Mounted on Cantilevers for High-Aspect-Ratio High-Resolution Imaging. *Nano Lett.* **16**, 6896-6902, (2016).

21   Sonntag, M.D. *et al.* Single-molecule tip-enhanced Raman spectroscopy. *J. Phys. Chem. C* **116**, 478-483, (2011).

22   Nie, S. & Emory, S.R. Probing single molecules and single nanoparticles by surface-enhanced Raman scattering. *Science* **275**, 1102-1106, (1997).

23   Hildebrandt, P. & Stockburger, M. Surface-enhanced resonance Raman spectroscopy of Rhodamine 6G adsorbed on colloidal silver. *J. Phys. Chem.* **88**, 5935-5944, (1984).

24   Hayazawa, N., Inouye, Y., Sekkat, Z. & Kawata, S. Near-field Raman scattering enhanced by a metallized tip. *Chem. Phys. Lett.* **335**, 369-374, (2001).

25   Watanabe, H., Hayazawa, N., Inouye, Y. & Kawata, S. DFT vibrational calculations of rhodamine 6G adsorbed on silver: analysis of tip-enhanced Raman spectroscopy. *J. Phys. Chem. B* **109**, 5012-5020, (2005).

26   Jensen, L. & Schatz, G.C. Resonance Raman scattering of rhodamine 6G as calculated using time-dependent density functional theory. *J. Phys. Chem. A* **110**, 5973-5977, (2006).

27   Yano, T.-a. *et al.* Tip-enhanced nano-Raman analytical imaging of locally induced strain distribution in carbon nanotubes. *Nat. Commun.* **4**, 2592, (2013).

28   Piscanec, S., Lazzeri, M., Robertson, J., Ferrari, A.C. & Mauri, F. Optical phonons in carbon nanotubes: Kohn anomalies, Peierls distortions, and dynamic effects. *Phys. Rev. B* **75**, 035427, (2007).

29   Yano, T.-a., Inouye, Y. & Kawata, S. Nanoscale uniaxial pressure effect of a carbon nanotube bundle on tip-enhanced near-field Raman spectra. *Nano Lett.* **6**, 1269-1273, (2006).

30   Benz, F. *et al.* Single-molecule optomechanics in "picocavities". *Science* **354**, 726-729, (2016).

31   Duan, X. *et al.* Resonant Raman spectroscopy of individual strained single-wall carbon nanotubes. *Nano Lett.* **7**, 2116-2121, (2007).

32   Picquart, M. Vibrational model behavior of SDS aqueous solutions studied by Raman scattering. *J. Phys. Chem.* **90**, 243-250, (1986).

nature
photonics

Article metrics for:

High external-efficiency nanofocusing for lens-free near-field optical nanoscopy

Last updated: Fri, 30 Aug 2019 20:21:09 GMT

Total citations

3712	0	0
Article Accesses	Web of Science	Crossref
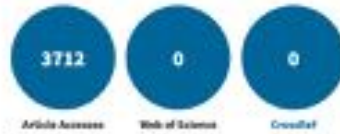
Online attention

Altmetric score (what's this?)

60

This Altmetric score means that the article is:

- in the 84th percentile (ranked 6,844th) of the 346,331 tracked articles of a similar age in all journals.
- in the 64th percentile (ranked 8th) of the 52 tracked articles of a similar age in Nature Photonics.

Mentions in news, blogs & Google+

News articles (8)

Fiber-optic probe can see molecular bonds
Phys.org

Fiber-optic probe can see molecular bonds
EurekAlert!

Fiber-optic probe can see molecular bonds
Nanowerk

Fiber-optic probe can see molecular bonds
Science Daily

nature
photonics

Fiber-optic probe can see molecular bonds
Chem Europe

Nanoscale optical imaging gets simpler and cheaper
physicsworld.com

Fiber-optic probe can see molecular bonds
New Electronics

Twitter demographics

Brazil	1	33.33%
Mexico	1	33.33%
No location data	1	33.33%

Explanation of terms and methodology

Sources
Web of Science, Crossref and Altmetric

Citations
Single number count for article citations from each service's database may vary by service. The citation counts are reliant on the availability of the individual RIN from Web of Science and Crossref. These counts are updated daily once they become available. Once a citation count is available, the list of articles citing this one is accessible by clicking on the circle for that citation source.

News, blogs and Google+ posts
The number of times an article has been cited by individual mainstream news sources, blog post, or member of Google+ along with a link to the original article or post. News articles, blog posts and Google+ posts do not always link to articles in a way that can be picked up by aggregators used by Altmetric, so the listed links are not necessarily a reflection of the entire scope of media, blog or Google+ interest. Further, the list of blogs and news sources covered is manually curated by Altmetric and thus is subject to their discretion for inclusion as a scientific blog or media source. The news, blog, and Google+ posts are provided by Altmetric and are updated hourly.

Altmetric score
Altmetric calculates a score based on the online attention an article receives. Each coloured thread in the circle represents a different type of online attention and the number in the centre is the Altmetric score. The score is calculated based on two main sources of online attention: social media and mainstream news media. Altmetric also tracks usage in online reference managers such as Mendeley and CiteULike, but these do not contribute to the score. Older articles will typically score higher because they have had more time to get noticed. To account for this, Altmetric has included the context data for articles of a 'similar age' (published within 6 weeks of either side of the publication date of this article).

For a more detailed description of Altmetric, the Altmetric score, and sources used, please see Altmetric's information page.

Twitter demographics
Provides the number of tweets broken down by country of origin for the Twitter account. The geographic breakdown for the twitter sources is provided by Altmetric and is updated hourly.

Back to article page »

natureresearch

About us   Press releases   Press office   Contact us

Discover content
Journals A-Z
Articles by subject
Nano
Protocol Exchange
Nature Index

Publish with us
Guide to Authors
Guide to Referees
Editorial policies
Open access
Reprints & permissions

Researcher services
Research data
Language editing
Scientific editing
Nature Masterclasses
Nature Research Academies

Libraries & institutions
Librarian service & tools
Librarian portal
Open research

Advertising & partnerships
Advertising
Partnerships & Services
Media kits
Branded content

Career development
Nature Careers
Nature Conferences
Nature events

Regional websites
Nature China
Nature India
Nature Japan
Nature Korea
Nature Middle East